

## Template AASTEXArticle with Examples: v6.3.1\*

1 GENGHAO LIU ,<sup>1</sup> YUNWEI DENG,<sup>2</sup> HUI LI,<sup>2</sup> BAITIAN TANG,<sup>3</sup> LIUBIN PAN,<sup>3</sup> LONG WANG,<sup>3</sup> HONGWEI GE,<sup>4</sup> AND  
2 ALISON SILLS<sup>5</sup>

3 <sup>1</sup>*School of Astronomy and Astrophysics, Sun Yat-sen University, Tangjiaawan, Xiangzhou, Zhuhai, Guangdong, China*

4 <sup>2</sup>*TsingHua University, Haidian DS 100084, Beijing, China*

5 <sup>3</sup>*School of Astronomy & Astrophysics, Sun Yat-sen University, Tangjiaawan, Xiangzhou, Zhuhai, Guangdong, China*

6 <sup>4</sup>*Yunnan Observatories, Chinese Academy of Sciences, Kunming 650216, People's Republic of China*

7 <sup>5</sup>*Department of Physics & Astronomy, McMaster University, 1280 Main Street West Hamilton, L8S 4M1, Canada*

### ABSTRACT

This example manuscript is intended to serve as a tutorial and template for authors to use when writing their own AAS Journal articles. The manuscript includes a history of AASTEX and includes figure and table examples to illustrate these features. Information on features not explicitly mentioned in the article can be viewed in the manuscript comments or more extensive online documentation. Authors are welcome replace the text, tables, figures, and bibliography with their own and submit the resulting manuscript to the AAS Journals peer review system. The first lesson in the tutorial is to remind authors that the AAS Journals, the *Astrophysical Journal* (ApJ), the *Astrophysical Journal Letters* (ApJL), the *Astronomical Journal* (AJ), and the *Planetary Science Journal* (PSJ) all have a 250 word limit for the abstract<sup>a)</sup>. If you exceed this length the Editorial office will ask you to shorten it. This abstract has 161 words.

**Keywords:** Classical Novae (251) — Ultraviolet astronomy(1736) — History of astronomy(1868) — Interdisciplinary astronomy(804)

### 1. INTRODUCTION

Globular clusters (GCs) are massive, dense, and ancient stellar systems that orbit galactic nuclei and serve as fossil records for the early phases of galaxy formation and chemical evolution (Raffaele G. Gratton et al. 2012; Gratton et al. 2004; Milone & Marino 2022; Renaud 2018; Gratton et al. 2019; Renzini et al. 2015). High-precision photometry and spectroscopy have revealed that stars within individual GCs are not chemically and/or temporally homogeneous: instead, most clusters host so-called multiple populations (MPs), typically split into a first population (1P) with composition similar to field stars and an enriched second population (2P) characterized by enhanced He, N, Na, Al and depleted C, O. The MP phenomenon manifests observationally as correlated light-element abundance patterns (e.g. C–N, Na–O, Mg–Al anti-correlations), systematic variations along the horizontal branch (HB), and multiple or broadened sequences in colour–magnitude diagrams (CMDs) and chromosome maps (?????).

Any viable MP formation theory must simultaneously reproduce these chemical signatures, their correlations with cluster global properties (mass, luminosity, orbital parameters), and internal structural and kinematic differences between 1P and 2P stars. Two observational constraints impose particularly strong, and often competing, requirements on formation mechanisms: the temporal constraints on when enrichment and second-generation star formation can occur (time budget), and the amount of enriched material required relative to available stellar mass (mass budget). Below we summarize these constraints and discuss their implications for proposed formation channels, with particular emphasis on massive interacting binaries as a promising route.

Mass budget constraints The mass budget problem is twofold. Internally, 2P stars typically constitute  $\sim$ 30–70% of present-day cluster members, so the amount of polluted material required is substantial. Externally, constraints from Galactic archaeology imply that present-day GCs could not have been orders of magnitude more massive at birth;

\* Released on March, 1st, 2021

<sup>a)</sup> Abstracts for Research Notes of the American Astronomical Society (RNAAS) are limited to 150 words

realistic bounds typically limit initial masses to at most a few times (e.g.  $\lesssim 5$ ) the current masses. Consequently, scenarios that explain high 2P fractions by invoking extreme preferential loss of 1P stars or highly abnormal initial mass functions (IMFs) are disfavoured unless additional, independent evidence supports such dramatic early mass loss (??).

Time budget constraints Observations of young massive clusters (YMCs) and direct searches for intra-cluster gas place stringent limits on the time available for producing, retaining and converting polluted gas into 2P stars. YMCs with ages of a few Myr generally show little or no evidence for extended or multiple bursts of star formation; for clusters up to  $\sim 10^5 M_\odot$  there is no robust evidence for age spreads larger than  $\sim 20\text{--}30$  Myr (??). Moreover, ionized, warm or cold gas reservoirs within clusters are observationally constrained to be very small (ionized gas  $< 10^2 M_\odot$  in many cases) beyond a few Myr after formation, and dense molecular gas is rapidly removed by feedback processes (?). In short, any enrichment mechanism that relies on slow return of processed material must either operate and produce sufficient ejecta on Myr time-scales compatible with rapid gas clearing, or supply material in a form and at locations where it can be efficiently retained and converted into stars before being removed.

Implications for formation scenarios These time and mass budget constraints severely limit the parameter space for MP formation models. Classical single-channel proposals exhibit distinct tensions: the AGB scenario benefits from slow, relatively cool winds that are easily retained, but AGB ejecta are released after  $\sim 30\text{--}300$  Myr and can struggle to reproduce the observed Na–O anticorrelation without finetuned dilution and mixing; FRMS (fast-rotating massive star) and supermassive/very-massive star (SMS/VMS) models produce appropriate abundance patterns more rapidly, but they rely on very massive stellar products and may produce too high He or require special conditions for retention of rapidly ejected winds (??). Many single-channel models also require either anomalous IMFs or large-scale loss of unenriched stars to meet the observed 2P fractions, which conflicts with the external mass-budget limits.

Advantages of massive interacting binaries Massive interacting binaries (MIBs) provide several key advantages when evaluated against the time and mass budget constraints. During non-conservative mass transfer and Roche-lobe overflow (RLOF), binaries can eject significant amounts of slow, chemically processed material on short time-scales (from a few Myr up to tens of Myr), i.e. well within the observational windows imposed by YMCs and gas-clearance limits. Simulations and binary-evolution calculations show that close massive binaries can shed large portions of the primary’s envelope, producing ejecta enriched in He, N, Na and Al and depleted in C and O—chemical signatures closely matching those observed in 2P stars (??). Importantly, the velocity of binary ejecta can be relatively low compared to supernova-driven flows, increasing the likelihood that the material remains bound to the cluster potential and can be incorporated into new stars.

From a mass-budget perspective, interacting binaries naturally supply a non-negligible fraction of cluster mass in processed ejecta. Estimates indicate that slow binary mass loss can constitute a substantial fraction of the original stellar mass budget (the user-provided estimate of  $\sim 13\%$  for certain binary channels is illustrative), and extending the donor mass range down to intermediate masses (e.g.  $\sim 4\text{--}9 M_\odot$ ) can further increase the available polluted mass without invoking exotic IMFs. Thus, MIBs reduce or remove the need to assume extreme early loss of 1P stars and are compatible with conservative limits on initial cluster masses.

Moreover, binaries naturally produce a range of yields and local dilution conditions: different binary periods, mass ratios and evolutionary states yield a variety of chemical signatures and ejection epochs, offering a plausible route to the observed spread and correlations among light elements and to heterogeneous He enrichment within a cluster. Binary interactions also provide a physical mechanism to generate rapidly rotating secondaries, contribute to stellar mergers, and seed environments where additional channels (e.g. FRMS, VMS, or AGB) could act in concert—supporting a hybrid, multi-channel formation picture without violating time or mass constraints.

Remaining challenges and path forward Despite these strengths, the binary channel is not a panacea. Quantitative comparison with observations requires robust binary population synthesis tied to cluster-scale hydrodynamics to predict retention efficiencies, dilution with residual or externally accreted gas, and the resulting star-formation efficiency for 2P stars. Uncertainties in binary fraction as a function of environment, the role of dynamical interactions in dense proto-cluster cores, and detailed nucleosynthetic yields across parameter space must be addressed.

In this work we therefore adopt a strategy that couples detailed binary-yield calculations with high-resolution hydrodynamical and dynamical modelling of proto-cluster environments. By explicitly tracking the timing, kinematics and composition of binary ejecta together with gas removal and star-formation physics, we aim to test whether interacting binaries—alone or in combination with other channels—can satisfy the stringent time-budget and mass-

92 budget constraints while reproducing the chemical and structural fingerprints of multiple populations in globular  
93 clusters.

94 Why hydro simulation? Why Binary?

## 95 2. METHODS

96 Simulations in this work are all performed on the framework of Arepo-RIGEL(Deng et al. 2024, Hereafter ), Arepo  
97 is a moving-mesh, finite-volume quasi-Lagrangian hydrodynamic code. Conserved variables in each Voronoi cell are  
98 evolved with a second-order, unsplit Godunov scheme; the cells can be refined and de-refined to meet resolution  
99 requirements, and the mesh-generating points (the seed that define the Voronoi tessellation) are free to follow the  
100 motion the fluid. AREPO therefore integrates the strengths of both grid-based and particle-based hydrodynamic  
101 methods and has already been applied to various astrophysical problems(Springel 2010; Vogelsberger et al. 2013;  
102 Weinberger et al. 2020; Torrey et al. 2012).

103 The RIGEL (Realistic ISM modeling in Galaxy Evolution and Lifecycles) model integrates individual massive-star  
104 feedback into AREPO-RT to model heating, cooling and chemical enrichment of the multiphase ISM. The radiation  
105 field is modeled in seven spectral bins ranging from IR to He II ionizing bands and used to evolve non-equilibrium  
106 chemistry of main ISM coolants (e.g., H, H<sub>2</sub>, C, O, CO) and compute, in real time, all coupled heating and cooling  
107 processes to produce a self-consistent per-cell net cooling rate. This enables RIGEL to capture the thermodynamics  
108 across all ISM phases, thereby simulating the entire process of star formation and feedback.

109 In the rest of this section, we demonstrate how to construct binary yield model base on Arepo-RIGEL.

### 110 2.1. *Binary Yield Model*

111 We sample binaries in Arepo-RIGEL using Primary-constrained pairing algorithm(Cournoyer-Cloutier et al. 2021):  
112 Once a star particle host a massive stars with mass  $M = M_{fb}$ , we draw a Uniform(0,1) random number and judge if  
113 it's smaller than a mass-dependant bianry fraction  $F(M_{fb})$  to determine whether this massive star has an companion.  
114 If does, the period  $P$  and mass ratio will be sampled sequentially. The probability of a binary system in a stellar  
115 population having a specific primary mass  $M_1 = M_{fb}$ , period  $P$  and mass ratio  $q = \frac{M_1}{M_2}$  is

$$116 F(M_1, P, q) = F(M_1)F(P|M_1)F(q|M_1P) \quad (1)$$

117 , where  $F(M_1)$  is primary-mass-dependant binary fraction distribution,  $F(P|M_1)$  is primary-mass-dependant period  
118 distribution,  $F(q|M_1P)$  is primary-mass- and period-dependant mass ratio distribution. All these three distributions  
119 are based on the observational results from Moe & Di Stefano (2017), the detailed sampling procedure is shown in  
120 Appendix A. The parameter space of the binary population covers all the massive star mass sampled by RIGEL( $M_1 \in$   
121  $[8M_\odot, 100M_\odot]$  is set in this work), period in log scale ranging 0.2-8, mass ratio ranging 0.1-1.

122 Mass transfer initiates when the primary star fills its Roche lobe (Chen et al. 2024). Chemically enriched gas is then  
123 transferred through the L1 Lagrangian point toward the secondary star, and ultimately expelled into the interstellar  
124 medium (ISM) due to the secondary's rapid rotation (De Mink et al. 2009). Approximately 80%-90% of the mass  
125 transfer is Case B mass transfer, i.e. the primary reaches the Roche limit before the onset of core helium burning(Van  
126 Den Heuvel 1969). We therefore define the onset of chemical enrichment as the time when the primary reaches the  
127 base of the giant branch (BGB), adopting the BGB timescale from Hurley et al. (2000):

$$128 t_{\text{BGB}}(M, Z) = \frac{a_1 + a_2 M^4 + a_3 M^{5.5} + M^7}{a_4 M^2 + a_5 M^7}, \quad (2)$$

129 with coefficients  $a_i$  ( $i = 1, 2, 3, 4, 5$ ) provided in Appendix A (Table 2).

130 In RIGEL, massive stars are assumed to evolve instantaneously, with supernova ejecta released only at the end of  
131 their lifetimes (Vogelsberger et al. 2013; Deng et al. 2024). Accordingly, we adopt  $t_{\text{BGB}}$  as the RLOF yielding timescale.  
132 Once the age of a massive interacting binary reaches this timescale, it releases all its enriched ejecta into the ISM. The  
133 chemical yields are derived through interpolation from the binary yield tables presented by Michelle Nguyen & Sills  
134 (2024), which were computed using the MESA stellar evolution code (Paxton et al. 2019).

135 The interpolated ejected mass table of binaries in this work is shown in Figure 1. Note that the parameter space  
136 of the binary population we sampled extends beyond existing chemical yield tables (See Fig 2 and Fig 1). For binary  
137 systems outside the tabulated ranges, we avoid extrapolation and instead introduce a 'boost factor' parameter to scale  
138 the ejecta mass. This addresses potential underestimation of binary enrichment due to incomplete parameter coverage

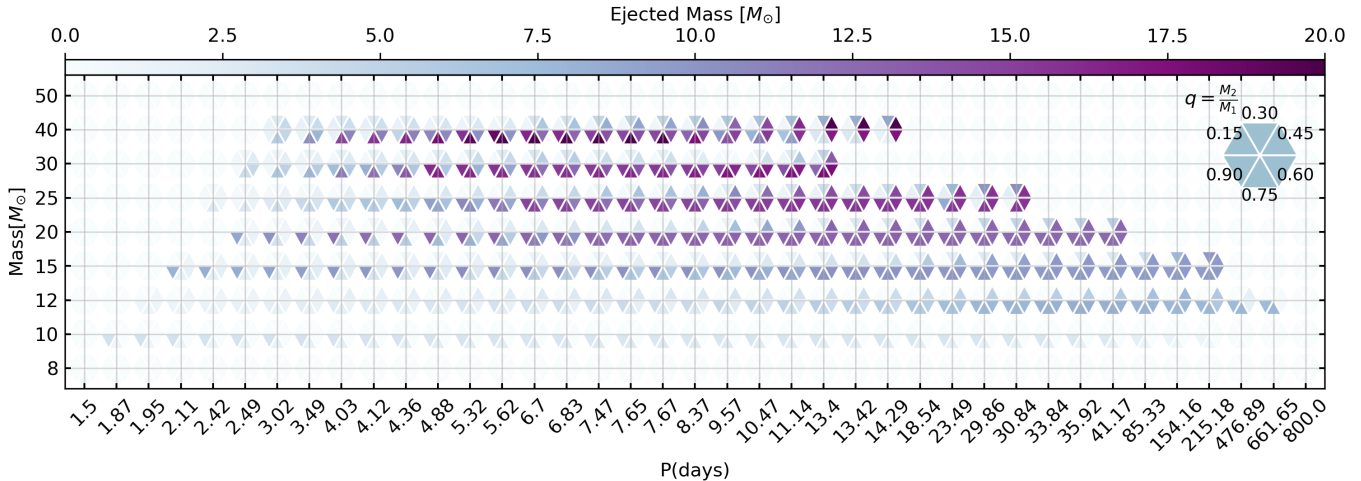


**Figure 1.** Interpolated ejected-mass table used in this work. Color scale shows the mass ejected by interacting binaries across the sampled parameter space. Horizontal axis: orbital period (log scale); vertical axis: primary mass. Each hexagon is subdivided into triangular wedges that encode different mass-ratio bins (legend at upper right). For example, the top-left triangular wedge denotes binaries with mass ratios in the range 0.15–0.30. The yields are interpolated from the MESA-based binary yield tables (see text); systems outside the tabulated ranges were treated using a boost factor to avoid extrapolation.

or omitted physical processes like common envelope ejection. The interpolated binary systems account for  $\sim \frac{1}{3}$  of the total mass of all binaries whose periods  $< 1500$  days, and  $\sim 14\%$  of the total sampled stellar mass (including single stars). These systems exhibit an average mass ejection fraction of  $\sim 23\%$ . Given that common envelope ejection typically releases  $\sim 80\%$  of its total mass, assuming the entire stellar population could enrich material at this rate would yield an estimated boost factor of  $\eta \sim 20$ , which is expected to be the upper limit of the whole population's enrichment capacity.

## 2.2. Post RLOF evolution

RIGEL assume that stars with initial masses between  $8 M_{\odot}$  and  $40 M_{\odot}$  explode by releasing  $\sim 1$  Bethe ( $1$  Bethe  $\equiv 10^{51}$  erg) thermal energy. However, binary interactions could significantly change the evolutionary path of the stars and lead to the discrepancy of the timing, intensity, and spatial distribution of stellar feedback and chemical enrichment (e.g. Laplace et al. 2021; Vartanyan et al. 2021; Wagg et al. 2025).

### 2.2.1. Mass transfer criteria

Mass transfer and its stability determine the fates of the binary (Chen et al. 2024; Soberman & Phinney ???; Temmink et al. 2023). The stability of the mass transfer are determined by the response of the primary radius under certain conditions to mass transfer versus the response of the roche lobe radius, which are

$$\zeta_{ad} = \left( \frac{d \ln R}{d \ln M} \right)_{ad}, \zeta_{th} = \left( \frac{d \ln R}{d \ln M} \right)_{th}, \zeta_L = \frac{d \ln R_L}{d \ln M}, \zeta_{L2} = \frac{d \ln R_{L2}}{d \ln M} \quad (3)$$

where  $R, R_L, R_{L2}$  denote radius of the donor(primary stars in this work), L1 point radius, L2 point radius, respectively, subscripts 'ad' and 'th' denote adiabatic and thermal equilibrium condition, repectively. Only when the radius of the primary contract more slowly or expand more rapidly than roche lobe raidius, i.e.  $\zeta_x(q) > \zeta_L(q)$  ( $x = ad, th$ )<sup>1</sup>, could mass transfer be sustainable. In our model, we employs three critical mass ratios  $q_{ad}, q_{th}, q_{L2}$ , which serve as the thresholds for triggering dynamical-timescale mass transfer, thermal-timescale mass transfer, and the overfilling of the outer Lagrangian surface (See Ge et al. 2010, 2020a, and the reference therein), to categorize the entire binary population into four distinct evolutionary channels. To distinguish between the conventional definition of mass ratio used in mass transfer studies and that employed in this work, we define the mass ratio in terms of the donor to accretor mass as  $\tilde{q} = \frac{M_{donor}}{M_{acc}} = \frac{1}{q}$ , then the four evolutionary pathways are classified as follow:

<sup>1</sup> Given conservative or constant fractional nonconservative mass transfer, mass–radius relations can be written only by the initial mass ratio  $q$ .

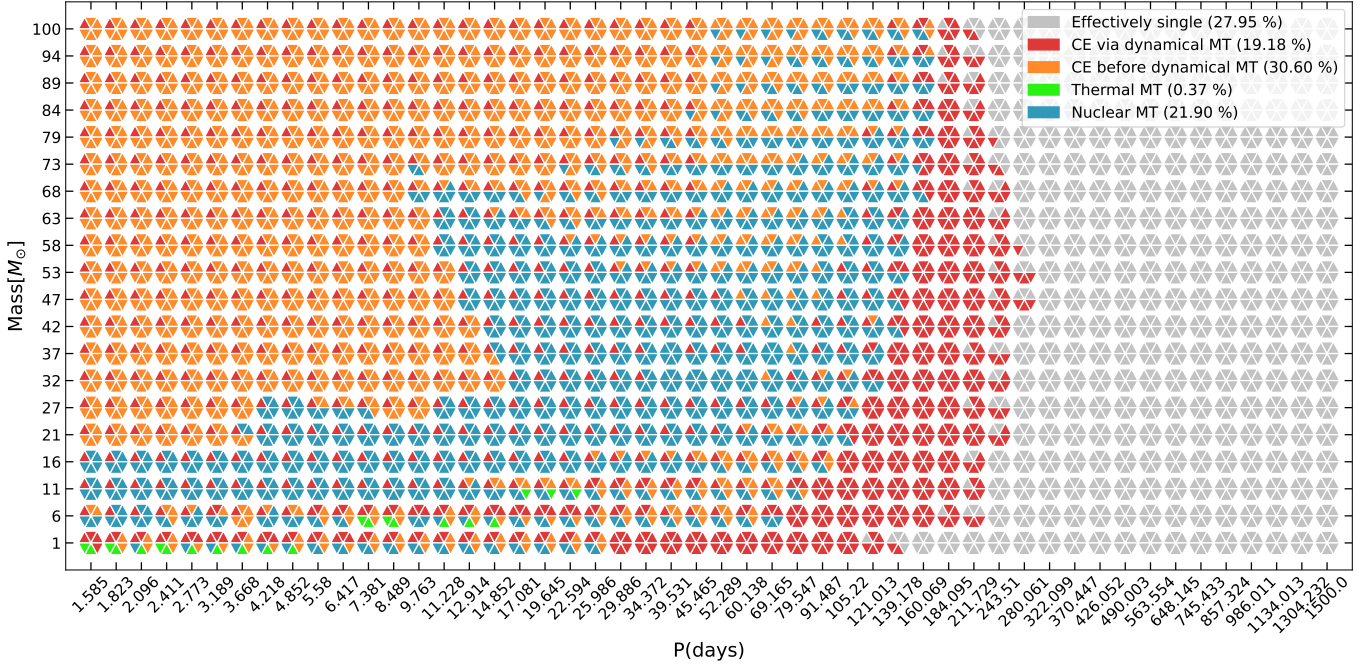


**Figure 2.** Map of mass-transfer timescales (dominant evolutionary channel) for binaries with orbital period  $P < 1500$  days. Regions are color-coded by the predicted timescale/channels determined by the critical mass ratios  $q_{ad}, q_{th}$  and  $q_{L2}$  adopted in this work (see Section 2.2.1 for detail).

- if  $\tilde{q} > q_{ad}$ , mass transfer will proceed on a dynamical timescale, and form a common envelope(CE) during mass transfer.
- if  $q_{L2} < \tilde{q} < q_{ad}$ , the mass transfer will be stable and proceeds on a thermal timescale with a common envelope formed by L2-overflow. This process will also form a CE.
- if  $q_{th} < \tilde{q} < \min(q_{L2}, q_{ad})$ , the mass transfer will be stable and proceeds on a thermal timescale. We assume this channel could form a binary-stripped star(He star) plus a accreted MS system.
- if  $\tilde{q} < q_{th}$ , the mass transfer will be stable and proceeds on a nuclear timescale. We assume this channel could also form a He+MS system.
- For those binary which will not interact before SNe, we expect that they do not have any differences with single stars, so our model treat them as single stars.

Critical mass ratio tables for thermal-timescale mass transfer and unstable mass transfer overfilling outer Lagrangian point are adopted from Ge et al. (2020b); Critical mass ratio tables for dynamical-timescale mass transfer are adopted from Ge et al. (2024), which cover fully conservative, semi-conservative, and fully non-conservative cases.

Binary-stripped stars, accreted MS companions, and CE systems including those undergoing subsequent CE ejection or coalescence, all deviate significantly from their primordial single-star evolution. However, a comprehensive, population-wide model that tracks their later evolution and quantifies their cumulative impact on stellar feedback and chemical enrichment is still lacking. In this work, we focus only on the environmental consequences of massive interacting binaries, rather than on the detailed fate of their remnants.

Accordingly, we assume that all primaries with masses between  $8M_\odot$  and  $40M_\odot$  will eventually undergo core-collapse supernovae. This assumption is justified because stars in this range generally form massive enough helium or carbon-oxygen cores to trigger either Type II or stripped-envelope (Ib/Ic) explosions, releasing comparable explosion energies. The upper bound of  $40 M_\odot$  is set by the onset of direct collapse into black holes in metal-poor massive stars (See similar implication from Xu et al. 2025; Heger et al. 2003), and the maximum mass in our model does not exceed the mass threshold for pulsational pair-instability(PPI Heger & Woosley 2002). The lower boundary, however, remains somewhat uncertain. For primaries with  $M_1 \in [8, 10]M_\odot$ . For their He+MS branch, the helium cores (typically

<sup>190</sup>  $\approx 2M_{\odot}$ ) lie close to or slightly below the empirical lower limits for the explodability of binary-stripped stars and  
<sup>191</sup> electron-capture supernovae (ECSN). Their subsequent fate depends sensitively on whether mass transfer occurs early  
<sup>192</sup> enough to prevent further core growth, or whether CE ejection leaves a remnant helium core too light to ignite  
<sup>193</sup> collapse. These marginal cases, represent a small fraction of our modeled binaries and thus have negligible impact on  
<sup>194</sup> the integrated feedback budget.

<sup>195</sup> The key role of binary evolution in our context is therefore not whether a supernova occurs, but when it occurs.  
<sup>196</sup> Binary interactions—through accretion, rejuvenation, or envelope stripping—can substantially modify stellar lifetimes  
<sup>197</sup> and delay or advance the onset of supernova feedback. Rejuvenation replenishes nuclear fuel in the core via rotational  
<sup>198</sup> or mixing processes, extending the lifetime of the primary (e.g., Wagg et al. 2025; Lynnette M. Dray & Christopher A.  
<sup>199</sup> Tout 2007; Schneider et al. 2016). Conversely, stripping produces a compact helium star with a steeper density profile  
<sup>200</sup> and different core compactness, affecting both explodability and explosion energy (Laplace et al. 2021; Vartanyan  
<sup>201</sup> et al. 2021; Gutcke et al. 2021; Steinwandel & Goldberg 2025). In the following subsection, we estimate the expected  
<sup>202</sup> supernova timescales for the different evolutionary channels considered in our model.

### 203 2.2.2. SNe timescale determination

<sup>204</sup> Binary interactions such as rejuvenation and envelope stripping can delay SN feedback in massive stars. The former  
<sup>205</sup> operates by replenishing the fuel supply of core’s nuclear reaction through internal chemical mixing, which in turn  
<sup>206</sup> extends the stellar lifetime (e.g., Wagg et al. 2025; Lynnette M. Dray & Christopher A. Tout 2007; Schneider et al.  
<sup>207</sup> 2016). The latter operates by producing a remnant envelope-stripped helium core with lower compactness and a  
<sup>208</sup> steeper density profile, which will also alter their explodability and SN energy (Laplace et al. 2021; Vartanyan et al.  
<sup>209</sup> 2021; Gutcke et al. 2021; Steinwandel & Goldberg 2025). In the next step, we are going to estimate the SNe timing  
<sup>210</sup> according to the remnant objects in different cases. Mergers-, accretion-, and rotation-induced chemical mixing can  
<sup>211</sup> cause stellar rejuvenation, to varying extents. For the merger in our model, we adopt the scheme of Glebbeek et al.  
<sup>212</sup> (2013)

$$\phi = C \frac{q}{(1+q)^2} \frac{R_{1,0.86} + R_{2,0.86}}{R_{1,0.5} + R_{2,0.5}} \quad (4)$$

$$f_{app} = \frac{1}{Q_c(M)} \frac{1}{1-\phi} \frac{Q_{c,1}f_1 + Q_{c,2}f_2q}{1+q} \quad (5)$$

$$t_{MS} = \tau_{MS} \left(1 - \frac{f_{app}}{\alpha}\right) \quad (6)$$

<sup>213</sup> where  $R_{n,0.86}$  and  $R_{n,0.5}$  are the radii containing 86 and 50 percent of the mass of parent star n (1 or 2). Here we  
<sup>214</sup> assume  $\frac{R_{1,0.86} + R_{2,0.86}}{R_{1,0.5} + R_{2,0.5}} = 1$  and  $C = 0.3, \alpha = 1.67$  for  $M < 2.4M_{\odot}$ ;  $C = 0.35, \alpha = 1.14$  for  $M >= 2.4M_{\odot}$  according to  
<sup>215</sup> Glebbeek et al. (2008); Schneider et al. (2016); Glebbeek et al. (2013). The comparasion of several  $Q_c$  value (Brott  
<sup>216</sup> et al. 2011; Sibony et al. 2024; Glebbeek et al. 2008) are shown in 3. We assume a fully mixed of the new stars and  
<sup>217</sup> hence we can derive a new metallicity by

$$Z_{\text{new}} = \frac{Z_{\text{old}}M_2 + M_{\text{He,acc}}}{M_2} \quad (7)$$

<sup>218</sup>, where  $Z_{\text{old}}$  is the metalicity before mass transfer,  $M_{\text{He,acc}}$  is the He mass of accreted mass.

<sup>219</sup> For accretion cases, the secondary will become primary in the new binary system if its mass exceed the previous  
<sup>220</sup> primary, and the new binary particle will inherit the age of its progenitor and rejuvenated following the scheme adopted  
<sup>221</sup> from Lynnette M. Dray & Christopher A. Tout (2007):

$$t' = \frac{M}{M'} \frac{\tau'_{MS}}{\tau_{MS}} t \quad (8)$$

<sup>222</sup> and the new metallicity will be estimated by

$$Z_{\text{new}} = \frac{Y + M_{\text{He,acc}}/M_2}{2 + 2M_{\text{acc}}/M_2} - 0.12 \quad (9)$$

<sup>223</sup>, where Y is the initial Helium abundance of the secondary.

<sup>224</sup> Thus, all massive binary stars will be updated into new stellar systems after BGB time according to their own binary  
<sup>225</sup> evolution channels, proceeding with subsequent evolution.

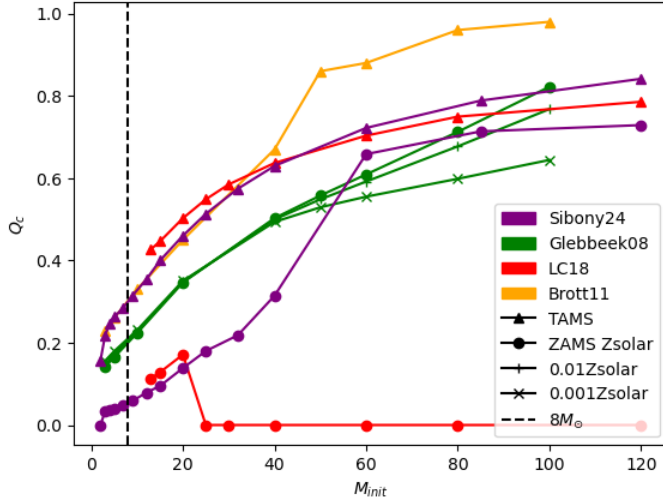


**Figure 3.** Comparison of core-mass fraction parameter  $Q_c$  from several stellar-evolution sources used in our rejuvenation prescriptions. Plotted curves/points show  $Q_c(M)$  from the different model grids, illustrating the variation in  $Q_c$  choices and motivating the range of values adopted in our merger/rejuvenation treatment.

### 3. INITIAL CONDITIONS

A series of initial GMCs were generated using MAKECLOUD(Grudić & Guszejnov 2021), exhibiting uniform density distributions and turbulent velocity fields characterized by identical power-law spectral indices consistent with the default configuration of MAKECLOUD. The molecular clouds were initialized in a sub-virial state characterized by virial parameters  $\alpha_0 \sim 0.8$ . Their dynamical evolution is governed by turbulent processes, featuring uniform density distributions and negligible initial rotation, such configuration is expected to promote internal mass redistribution from uniform to centralized distributions(Xu & Lazarian 2020; Murray et al. 2017; Murray & Chang 2015), ultimately leading to stellar formation through turbulent fragmentation. The turbulent spectrum follows a Kolmogorov-type scaling with spectral index 2.0, implemented through balanced solenoidal and compressive modes to replicate observed inertial-range turbulence. The gas temperature is initialized to 10 K, which is commonly used for GMC simulations(Li et al. 2019; McKee & Ostriker 2007; Julia Roman-Duval et al. 2010). The initial chemical composition adopts an alpha-enhanced abundance pattern following Michelle Nguyen & Sills (2024), characterized by metallicity parameters  $[\text{Fe}/\text{H}] = -1.44$ ,  $[\text{O}/\text{Fe}] = 0.44$ ,  $Z = 1.2 \times 10^{-3}$  and  $\text{Y} = 0.25$ .

We employ a RSLA(Reduced Speed of Light Approximation, see Gnedin & Abel 2001) factor of 0.001, i.e.  $\tilde{c} = 0.001c$ , to increase the efficiency without introducing numerical errors(Rosdahl et al. 2013). We also employ the spatial resolution correction methods outlined by Deng et al. (2023) to ensure the feedback effects converge correctly across different simulation resolutions.

All relevant physical parameters characterizing these initial conditions are tabulated in Table 1. We varied the masses and radii of the GMCs to explore the their relations to multiple stellar populations. Deng et al. (2024) enforced an instantaneous star formation when the length of the gas cell is larger than half of its local jeans length, i.e.  $m_{\text{gas}} > f_{j,s}^3 M_J$ , where  $f_{j,s} = 0.5$ , violation to which would cause the artificial fragmentation. There, we follow their settings and chose mass resolutions to ensuring all the gas cells would not violate that sufficient condition at the very beginning of the simulation. We mammally revise the yielding timescale with a yield lag "L", which denotes the time of yielding after their birth, and the enrichment from individual binary systems allows for amplification by a boost factor  $\eta$ (See 5 for details).

M1e6R15, SFH consistent but different [Na/Fe]

### 4. STAR FORMATION

In total, there are 18 GMC simulations varying with masses, radii, chemical yield boosting factors in our work. Each simulation stops when the star formation quenched, typically at  $\sim 2t_{ff}$ (See Li et al. 2019; Ni et al. ????, and Fig. 5).

A visualization of star cluster formation is shown in Figure 4. No global contraction is ovserved in this GMC during the whole star formation process, stars formed with the dense filament and fragments instead of center dense clumps,

**Table 1.** Initial conditions of GMCs.

Name	M M <sub>⊙</sub>	R pc	t <sub>ff</sub> Myr	ρ <sub>0</sub> M <sub>⊙</sub> /pc <sup>3</sup>	Σ <sub>0</sub> M <sub>⊙</sub> /pc <sup>2</sup>	α <sub>0</sub>	yield lag	η	Δm <sub>gas</sub> M <sub>⊙</sub>	
M1e7R15L0E1	1e7	15	0.29	707.36	3536.78	0.79	0	1	1.0	0.43
M1e7R30L0E5	1e7	30	0.83	88.42	884.19	0.78	0	20	2.0	0.38
M1e6R15L0E1alpha	1e6	15	0.93	70.74	353.68	0.77	0	1	0.5	0.23
M1e6R15L0E1newyt	1e6	15	0.93	70.74	353.68	0.78	0	1	0.6	0.25
M1e6R20L0E1	1e6	20	1.43	29.84	198.94	0.77	0	1	1.0	0.25
M1e7R50L0E5	1e7	50	1.79	19.10	318.31	0.77	0	20	9.1	0.49
M1e6R30L0E1alpha	1e6	30	2.63	8.84	88.42	0.79	0	1	1.0	0.21
M1e5R15L0E20	1e5	15	2.94	7.07	35.37	0.12	0	20	0.5	0.16
M1e6R50L0E1	1e6	50	5.66	1.91	31.83	0.79	0	1	1.0	0.16
M1e6R50L0E20	1e6	50	5.66	1.91	31.83	0.79	0	20	1.0	0.16
M1e7R200L0E1	1e7	200	14.31	0.30	19.89	0.78	0	1	1.0	0.12
M1e7R200L0E20	1e7	200	14.31	0.30	19.89	0.78	0	20	1.0	0.12
M1e6R100L0E1	1e6	100	16.00	0.24	7.96	0.79	0	1	1.0	0.11
M1e6R100L0E20	1e6	100	16.00	0.24	7.96	0.79	0	20	1.0	0.11
M1e5R50L0E20	1e5	50	17.89	0.19	3.18	0.00	0	20	1.0	0.11

NOTE—Column information from left to right: model name, initial GMC mass M, initial GMC radius R, initial free-fall time t<sub>ff</sub>, initial density ρ<sub>0</sub>, initial surface density Σ<sub>0</sub>, initial virial parameter for the rotational components α<sub>0</sub>, yield lag, Enrichment boost factor η, target mass for gas cells Δm<sub>gas</sub>.

this behavior is normal in uniform initial density profile, and is consistent with many simulations(e.g. Li et al. 2019; Shi et al. 2025; Birka Zimmermann et al. 2025). At ∼ 1.37 Myr, turbulent velocity field dominates the formation of complex filamentary structures, causing early star formation (white dots) along the filaments and within dense clumps at off-center locations(Upper left). At ∼ 2.64 Myr, the cloud furtherly collapses, the high-density regions are compressed further, and several stellar sub-clusters hierarchically form and merge, the star formation comes to its peak at this time. At ∼ 4.01 Myr, more sub-clusters form and merge at the center of the cloud complex, while the strong stellar feedback start to distroy filamentray structure. At ∼ 5.28 Myr, almost all the gas is expelled by the stellar feedback at this stage, filamentray structures are all destroyed, some bubbles are shown in lower right panel. The stars are color-coded by their [Na/Fe], 2P stars([Na/Fe]>0.3) will be marked as pure red, however they are too few(∼ 1%) to seen in this figure.

Figure 5 shows the star formation histories of the GMCs. Star formation histories for most of the GMCs are similar to Li et al. (2019). With the exception of extremely dense giant molecular clouds, all GMCs in this study exhibit star formation histories following a "triangle" pattern. This manifests as a linear proportionality between early star formation rate and time, aligning with the theoretical predictions by Murray & Chang (2015) regarding star formation evolution under self-gravity. Star formation duration τ<sub>dur</sub> ∼ 2t<sub>ff</sub>, and integrated star formation efficiency ε<sub>int</sub> of all GMCs are similar to what Li et al. (2019) predicted, despite their lacking of radiation feedback and SN feedback, which implies that those two factor might be affected by the type of feedback. The time when SFR start and their peaks might be sensitive to the initial surface densities.

Integrated ε<sub>int</sub> versus initial surface density is shown in Fig 6, red solid line with 68% confident range(shown in orange translucent band) is fitted using the formula in Li et al. (2019) and obtain the parameter f<sub>boost</sub> = 4.967<sup>+0.951</sup><sub>-0.803</sub>.

$$\epsilon_{\text{int}} = \frac{\sqrt{\Gamma^2 + (4\beta - 2)\Gamma + 1} - (2\beta - 1)\Gamma - 1}{2(1 - \beta)\Gamma}. \quad (10)$$

where Γ ≡ Σ<sub>sh</sub>/Σ<sub>crit</sub> = πGΣ<sub>0</sub>/4f<sub>boost</sub>̂p<sub>W</sub>, β = 1.83 ± 0.89 and p̂<sub>w</sub> = (3.32 ± 0.64) × 10<sup>-9</sup>cm/s<sup>2</sup>(See Li et al. 2019, for details).

$$\Sigma_{\text{crit}} = \frac{\dot{p}}{\pi G} = \frac{p_w f_{\text{boost}}}{\pi G} \quad (11)$$

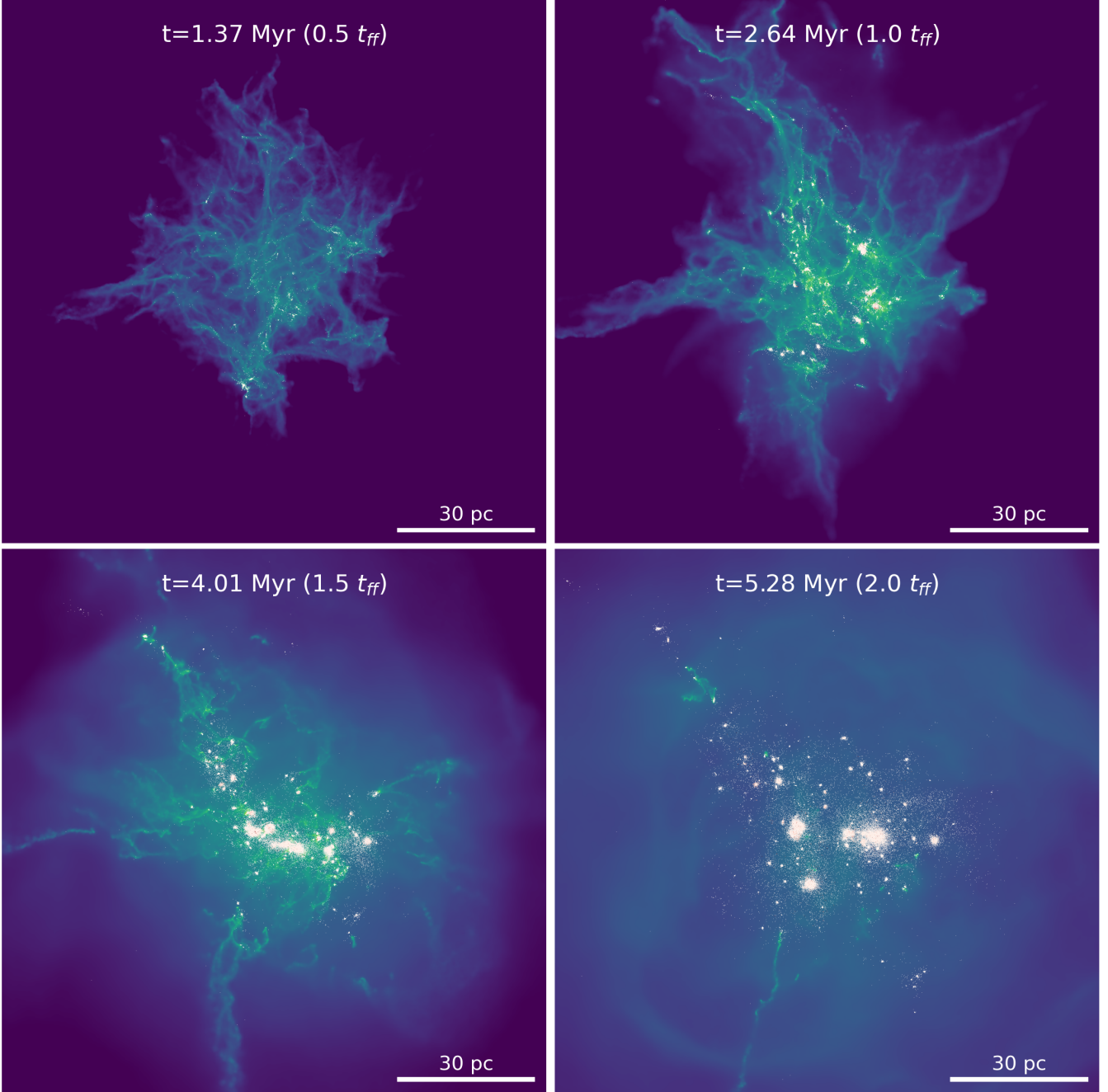


**Figure 4.** Four-panel visualization of star cluster formation in a representative GMC at successive times (upper-left to lower-right): 1.37 Myr, 2.64 Myr, 4.01 Myr, and 5.28 Myr. Panels show the gas/projected structure and star-particle locations; early star formation appears along filaments and in off-center dense clumps, sub-clusters form and hierarchically merge, and by the final time most gas has been expelled by feedback (bubbles visible). Star particles are color-coded by [Na/Fe]; 2P stars ( $[\text{Na}/\text{Fe}] > 0.3$ ) would be pure red but are too rare ( $\sim 1\%$ ) to be prominent in this visualization.

where  $p_w = 3.32 \times 10^9 \text{ cm/s}^2$  is the IMF- and time-averaged momentum deposition rate per unit mass, adopted from Li et al. (2019) fitted results;  $f_{\text{boost}}$  is a boosting factor of feedback. In the language of Lancaster et al. (2021a,b),  $\Sigma_{\text{crit}} = 4\Sigma_{\text{Edd}}$ , the 4 is originated from different definition of surface density, they are actually equivalent. And other formalisms are all equivalent (Fall et al. 2010; Murray 2011; Raskutti et al. 2016).

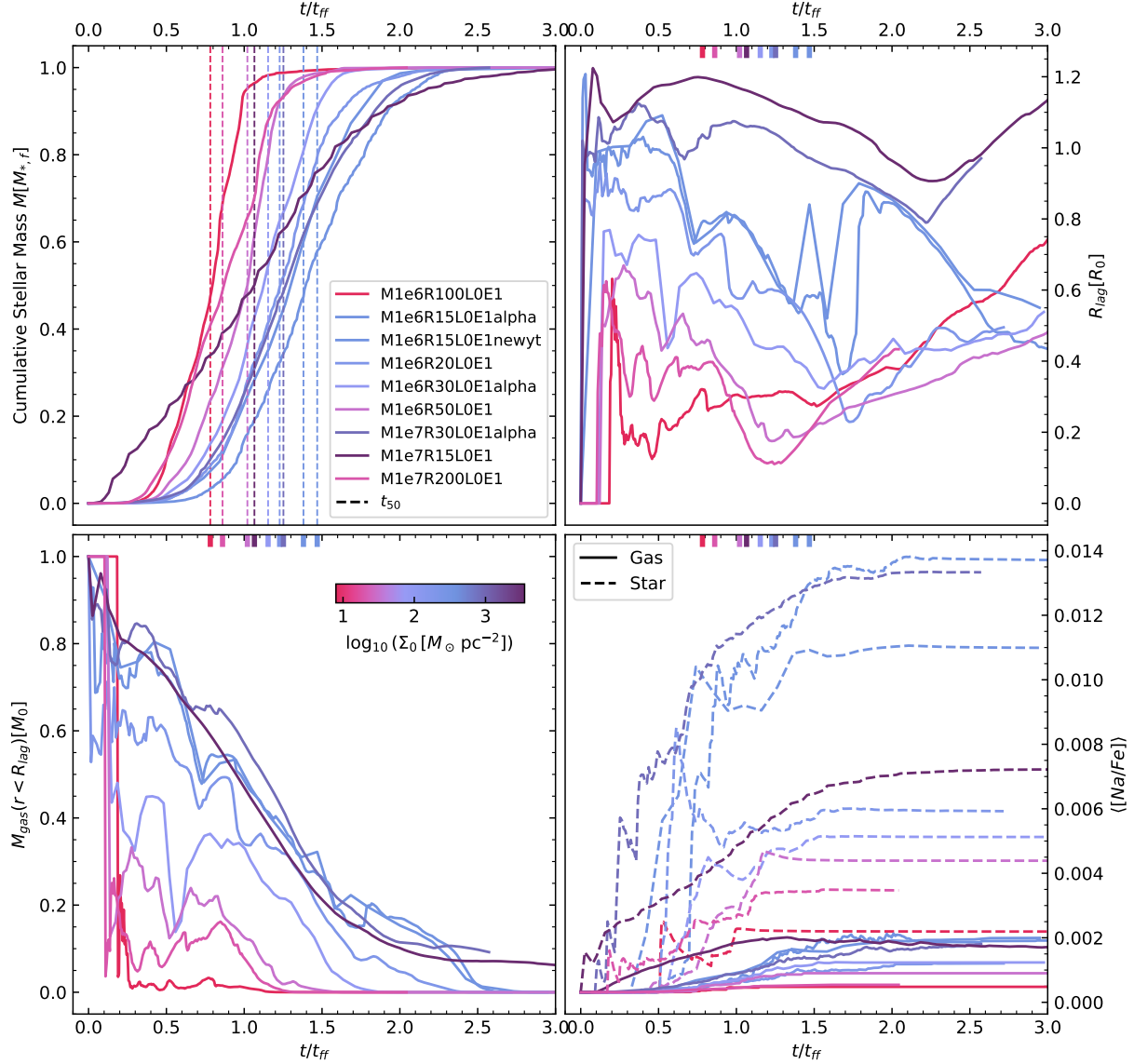


**Figure 5.** Star formation histories (SFR vs. time) for the suite of GMC simulations. Most runs show a 'triangle' pattern (linear rise to a peak near  $\approx t_{\text{ff}}$  followed by a decline), with typical star-formation durations  $\tau_{\text{dur}} \sim 2t_{\text{ff}}$ . Differences in onset time and peak are driven by initial surface density and other initial conditions (see text).

For GMC with surface density  $> 10^4 M_{\odot}/\text{pc}^3$ , the engagement of the star formation will be foreseen, but this is also a resolution issue, the mass of each particle is too close to the RIGEL's sufficient criterion (see [Deng et al. \(2024\)](#) for details), urging a star formation in advanced.

## 5. THE FORMATION OF SECOND POPULATION

### 5.1. Time Budget

Following the convention of previous observational and numerical studies (e.g., [Carretta et al. 2009](#); [Lahén et al. 2024](#)), we define 2P stars as those whose  $[\text{Na}/\text{Fe}] > 0.3$  dex. In our fiducial star formation simulations, we observe a complete absence of 2P stars formed. This null result is physically consistent with the anticorrelation between star formation duration (SFD) and star formation efficiency (SFE), a relationship well-documented in the literature ([Grudić et al. 2018](#); [Li et al. 2019](#); [Ostriker & Kim 2022](#)), etc. As is mentioned above, the average yielding timescale of the yield table is  $\sim 12$  Myr, with the earliest yielding timescale of  $\sim 6$  Myr. For the GMCs whose star formation duration is shorter than the minimum binary yielding timescale, The time it takes for a GMC to reach the peak of its

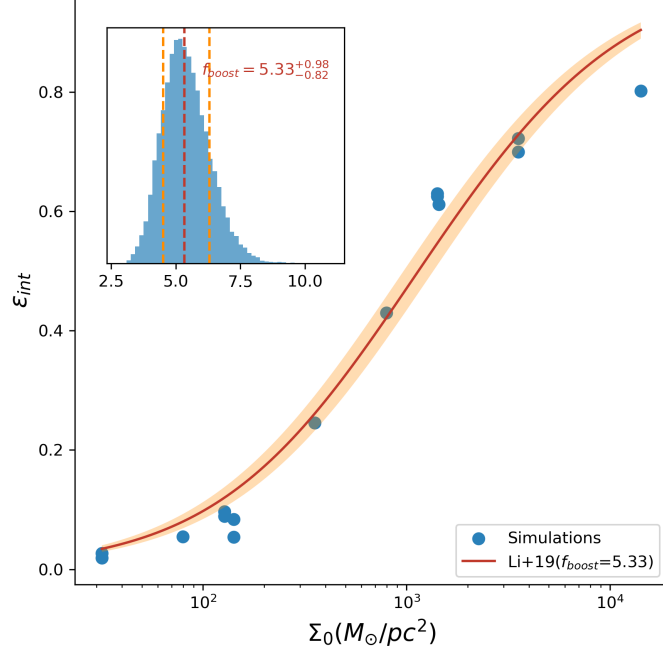


**Figure 6.** Integrated star-formation efficiency  $\epsilon_{int}$  for all runs as a function of initial gas surface density  $\Sigma_0$ . The red solid line is the fitted relation following Li et al. (2019) and the orange band shows the 68% confidence interval from the MCMC fit; the fitted boost parameter is  $f_{\text{boost}} = 4.967^{+0.951}_{-0.803}$ .

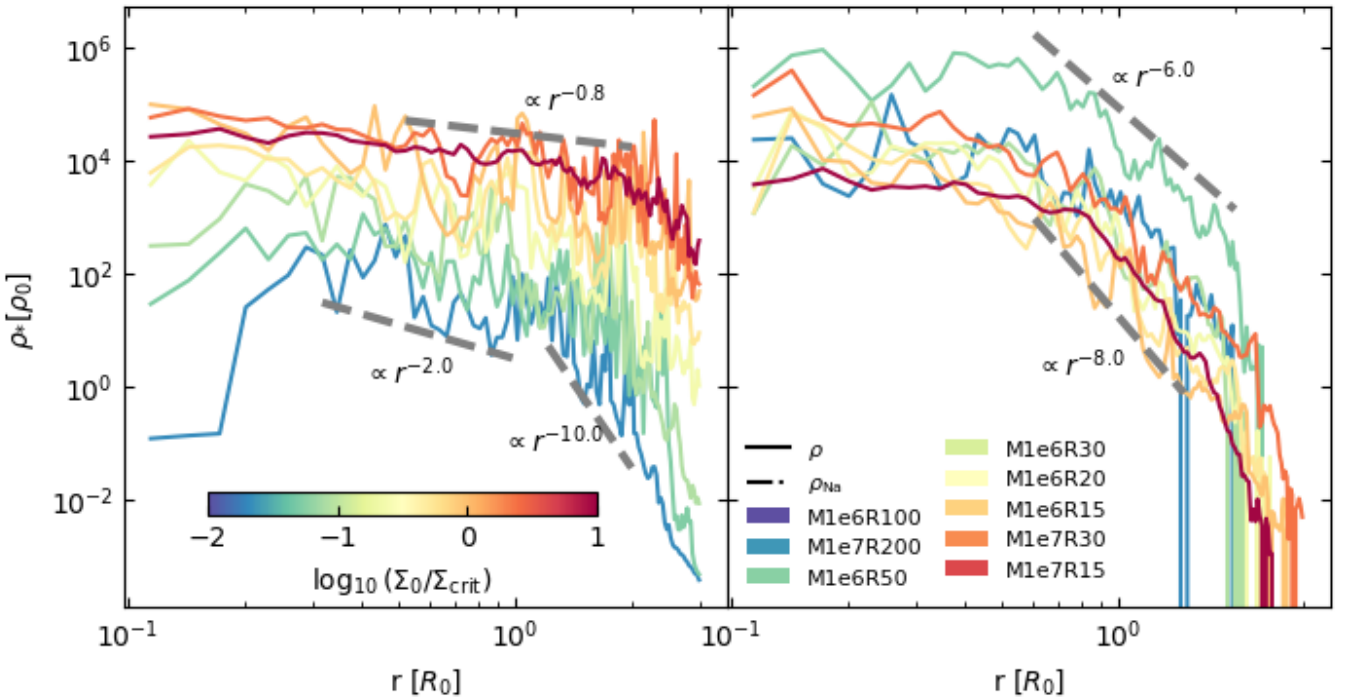


**Figure 7.** Enter Caption

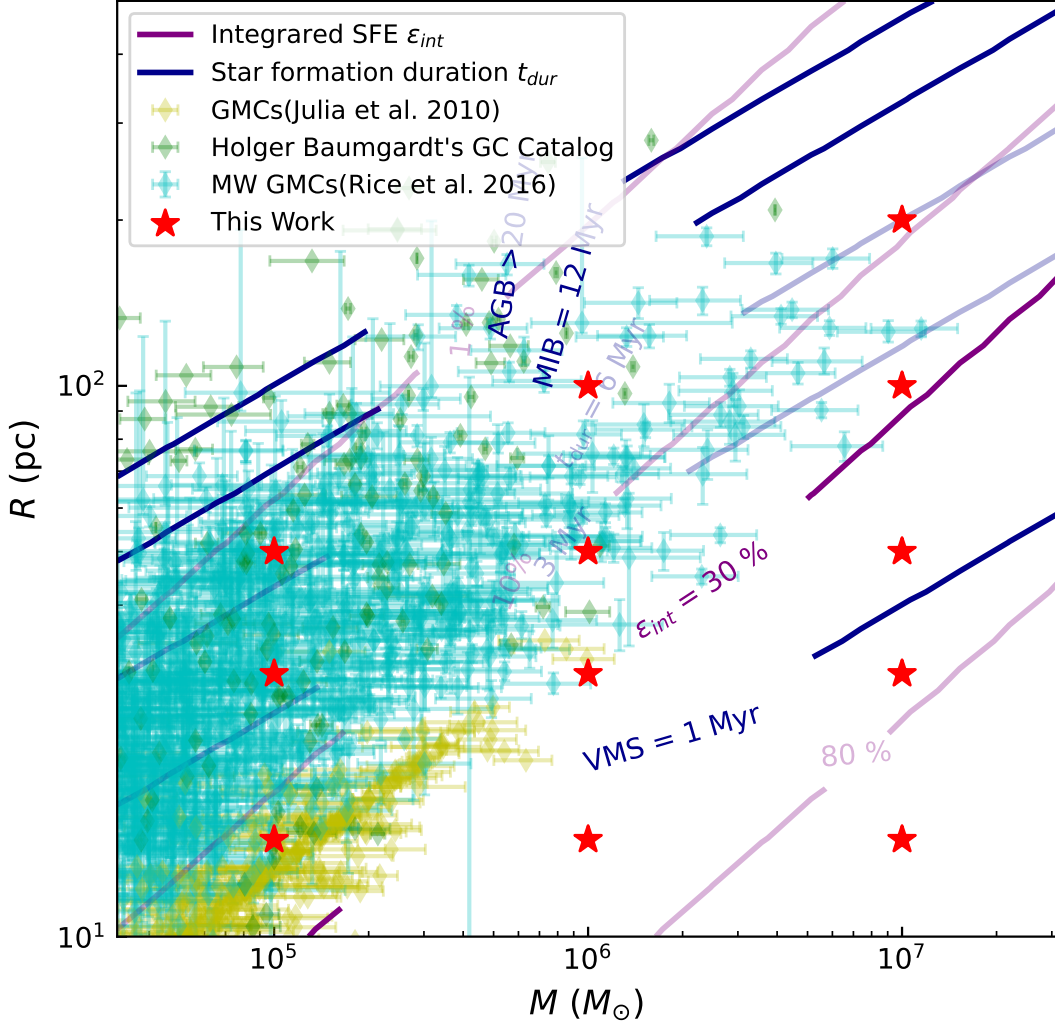


**Figure 8.** Initial parameter space for GMCs. Red contours: Integrated star formation efficiency  $\epsilon_{int}$ . Blue contour: Star formation duration  $\tau_{dur}$  and the corresponding yielding timescale of different scenarios(AGB,VMS,MIB).

star formation activity is approximately one free-fall time, and the star formation duration is about twice the free-fall time(Ni et al. ????). So we see at 3.2 Myr, the gas in GMC was expelled and star formation stop, but there's no 2P material released until about 6 Myr. And if the free fall time is larger than yielding time. here's an example, too few star formed in 6 Myr, so the enrichment in gas is not significant until 20 Myr.

Figure 8 demonstrates a so-called "Time Budget" dilemma: the mismatch between the star formation duration, star formation efficiency and the yielding timescale. Producing substantial 2P material demands higher SFE, but for isolated GMC, Denser clouds have higher SFE, it also lead to a shorter free fall time the stronger stellar feedback disrupts the cloud more rapidly, inevitably shortening the SFD. This shortened timescale leaves insufficient time window for the release and mixing of enriched ejecta with pristine gas, and its subsequent settling into new stars. The GMCs that can simultaneously satisfy high SFE, typical 30% in red countours and long SFD,like blue countours, this GMC must be extremely massive and large(See Figure 8).

However, the selection of star formation duration criteria is flexible, it depends on the mass of the the contamination sources, the more massive polluters yield earlier, which require looser GMC lifetime. In addition, SFD could be elongated by the impact of external forces, such as star formation under cloud-cloud collision, gas inflow conditions(Fukui et al. 2020; Maity et al. 2024; Glen H Hunter et al. 2023; Wu et al. 2017, 2015).

From that perspective, very massive stars(VMS, $\sim 10^2 M_\odot$ , using definition from e.g. Vink 2023), super massive stars(SMS, $\sim 10^3 M_\odot$ , Bastian & Lardo 2018) have short evolutionary timescales due to their high masses, resulting

in naturally short enrichment timescales and hence larger time window. Alternatively, other models such as binary interaction(Jiang et al. 2014), early disc accretion(Bastian et al. 2013), fast rotating stars(Decressin et al. 2007) may exhibit equivalent short yielding timescales under specific conditions, providing additional pathways to resolve the time budget dilemma.

In our study, we employ massive interacting binaries (MIB) as the primary enrichment source, which can inherently shorten the enrichment timescale through efficient mass transfer and binary interactions that accelerate ejecta release. The emergence of zero 2P stars in this work is not due to limitations of the MIB scenario itself, but rather arises from incomplete stellar evolution tables, insufficient coverage of mass ranges in the models, and constraints in computational resources. These factors reflect broader limitations in binary evolution theory and enrichment modeling. As mentioned in Section 3, we introduce a 'yield lag' parameter to explicitly control the enrichment timescale, enabling more flexible adjustment of the timing of ejecta incorporation. This approach sets the stage for the next section, where we detail the implementation of the yield lag parameter and its impact on simulation outcomes.

To maximize the enrichment time window, in some simulations, we artificially forced stars to release pollutants immediately upon their birth (marked as "L0") and boosted the yield mass by a factor of twenty (marked as "E20"; see Table 1 for details). The L0 setting aims to extend the time available for enrichment by eliminating delays, while E20 elevates the enrichment mass to the upper limit of the mass range, ensuring maximum material for 2P formation. These adjustments allow us to investigate the conditions that favor the incorporation of 2P gas into stars, which will be explored in the next chapter on mass budget, focusing on how specific parameters influence 2P enrichment efficiency.

## 5.2. Mass Budget

Figure 9 shows some basic properties of multiple populations in the newly formed star clusters. We expect that giant molecular clouds with tag "L0E20" and highest surface density will represents the upper limit of the number ratio of second-population (2P) stars. Note that star particles in RIGEL do not represent individual stars but rather subsets of the overall stellar population, the term "number of star particles" may be conceptually misleading. Therefore, we define the 2P ratio as the mass fraction of star particles with  $[\text{Na}/\text{Fe}] > 0.3$  relative to the total stellar mass, i.e.,

$$\text{2P ratio} = \frac{M_*([\text{Na}/\text{Fe}]_i > 0.3)}{M_*}$$

, if we assume 1P and 2P stars share the same mass function, this mass-based ratio is equivalent to the number ratio of 2P to total stars. Additionally, we introduce the mean stellar Na abundance as a continuous metric to quantify the amount of enriched gas that goes into stars, defined as

$$\langle [\text{Na}/\text{Fe}] \rangle_* = \lg \left( \frac{\sum_i N_{\text{Na},i}}{\sum_i N_{\text{Fe},i}} \right) - [\text{Na}/\text{Fe}]_\odot \quad (12)$$

, where  $N_{\text{Na},i}$  and  $N_{\text{Fe},i}$  are the total number of Na and Fe in  $i$ -th star particle, respectively. the 2P ratios still rarely exceeded  $\sim 6\%$  in isolated GMCs (See Fig. 9). If considered a typical star loss fraction of two-thirds(Baumgardt & Hilker 2018), 2P ratio is still much lower than the order of observations. The mean  $[\text{Na}/\text{Fe}]$  of the whole simulation suits ranging from 0.002 – 0.1 dex.

Figure 9 demonstrates the relation between the initial surface density and the mean stellar Na abundance. For those GMCs with surface density below the marked  $\Sigma_{\text{crit}}$  (dashed line), the rise in  $\langle [\text{Na}/\text{Fe}] \rangle$  is monotonic and gradually (from  $\sim 0.2$  at  $\Sigma_0 \sim 10 \text{ M}_\odot \text{pc}^{-2}$  to  $\sim 0.50.6$  at  $\Sigma_0 \sim 10^2 \text{ M}_\odot \text{pc}^{-2}$ ). A sharp leap of the trend and the maximum mean stellar Na abundance of this series of simulations appear at  $\sim \Sigma_{\text{crit}}$ . Note that this abundance leap is not coupled with surface density merely, because there is another GMC M1e7R47L0E1 which share the same  $\Sigma_0$  with the peak simulation M1e6R15L0E1 but remains slight increase compare to the lower  $\Sigma_0$  GMC. Error bars estimated by bootstrapping confirm the truly existence of this abundance peak. Deep connection linking the global IC of GMCs to the mean stellar Na abundance will be discussed in Section 6.

The stellar  $[\text{Na}/\text{Fe}]$ – $[\text{O}/\text{Fe}]$  distribution is characterized by a dominant 1P base at O enriched and Na depleted zone plus a extended enriched 2P tail; As is shown in Fig. ?? blue symbols denote the original enrichment scenario while red ones indicate the enrichment boosted by a factor of 20, and the red stars show the maximum, mean and minimum yielded  $[\text{Na}/\text{Fe}]$ ; the colored error bars and dash lines in the right histogram are the  $[\text{Na}/\text{Fe}]$  range predicted by instantaneous dilution model (see Section 6.1); Only one simulation M1e5R15L0E20 display a bimodal distribution in  $[\text{Na}/\text{Fe}]$ , and isolated clumps on Na-O plane, particularly at the high-Na end—rather than a single smooth locus, and

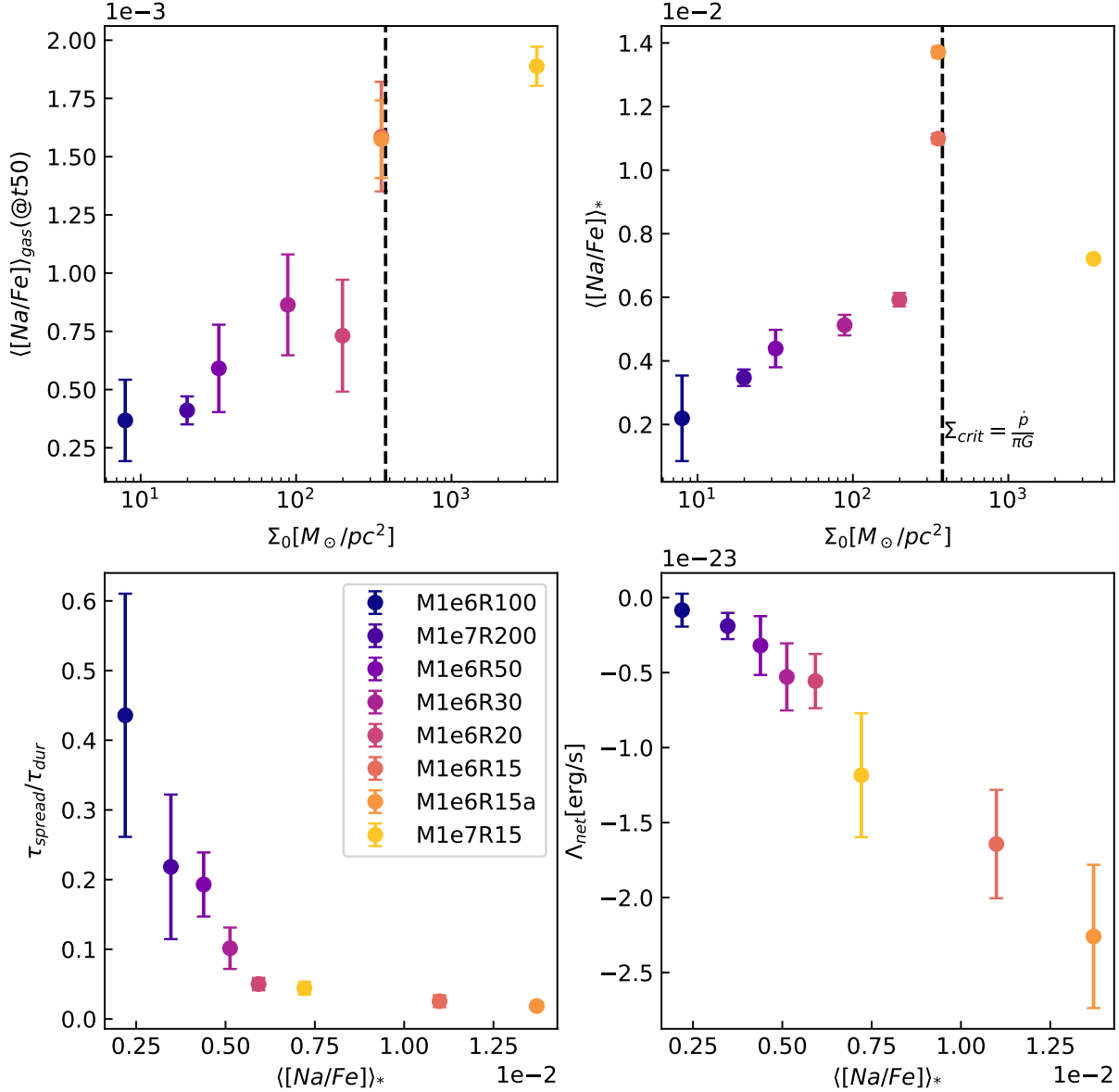


**Figure 9.** Summary of multiple-population metrics across the simulation suite. Plotted quantities include the 2P mass fraction (defined as mass fraction of star particles with  $[\text{Na}/\text{Fe}] > 0.3$ ) and the mean stellar  $[\text{Na}/\text{Fe}]$  as a function of initial surface density; runs with immediate yielding (L0) and boosted yields (E20) are highlighted. Error bars (where shown) are estimated via bootstrap. The figure demonstrates a peak in mean  $[\text{Na}/\text{Fe}]$  near the critical surface density  $\Sigma_{\text{crit}}$  (see text).

these discontinuities and local overdensities naturally arise when star formation samples both locally enriched pockets and the less-processed background because mixing proceeds from highly processed material toward the pristine baseline and is inefficient or patchy, producing bimodal or multi-peaked marginal distributions in Na as well as the observed discreteness.

First we have to make sure that the variations of mean stellar surface density are caused by the contingency due to the insufficient sampling of binaries. We did a bootstrap to resample the binaries of each simulations with a given total system number, the results shown in Fig ?? prove that the  $\langle [\text{Na}/\text{Fe}] \rangle_*$  discrepancies among GMCs are not merely caused by the random formation of contamination sources. The right panel implies that the sub-populations might be an important factor to the  $[\text{Na}/\text{Fe}]$ , which is similar to a so-called "Multi-Generational Cumulative Enrichment"

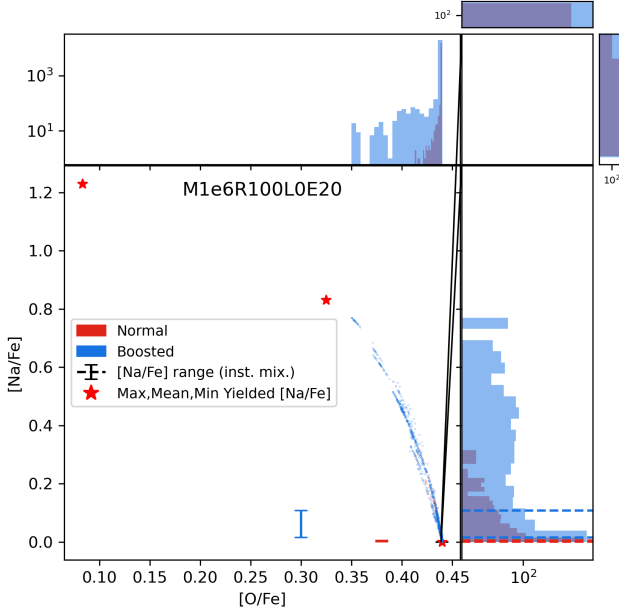


**Figure 10.** Na–O abundance distribution for simulation M1e6R100. Symbols/colors indicate the baseline enrichment scenario and boosted runs (blue: original yields; red: yields boosted by factor 20); red stars mark the maximum, mean and minimum yields from the yield tables. The distribution is dominated by a 1P locus with an extended 2P tail, illustrating spatially and temporally inhomogeneous enrichment.

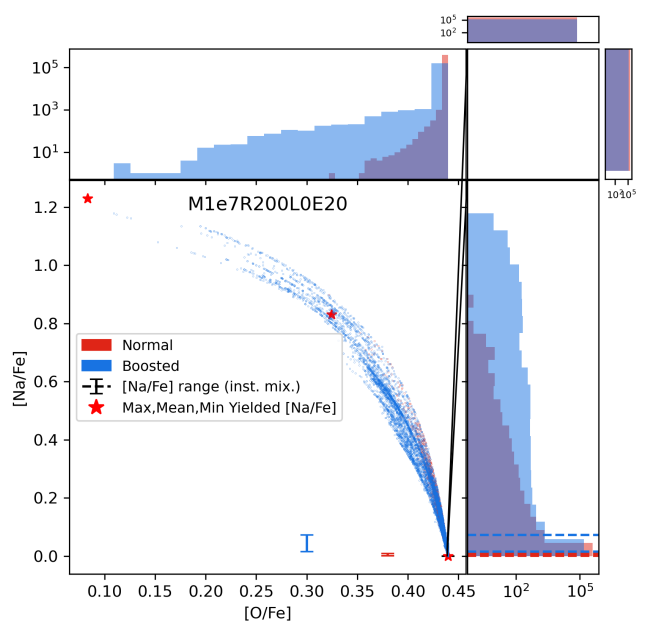


**Figure 11.** Na–O abundance distribution for simulation M1e7R200. As in the companion panel, blue points denote the original enrichment scenario and red points the boosted-yield case; annotations indicate yield-model extrema. The plot shows a dominant 1P population and an extended enriched tail rather than a single smooth locus.

372 proposed in Jenny J. Kim & Lee (2018). Given that knowledge, the formation of the first batch of enriched stars is  
 373 getting more important, that's to say, the mixing process in a very early time is important.

374

## 6. KEY DRIVERS OF MULTIPLE POPULATIONS FORMATION

375

### 6.1. Mixing Process

376

377

378

379

380

In previous literatures(Bastian et al. 2013), MP or its mass budget is calculated over a averaged level,i.e. comparing the total amount of 2P material to the pristine gas, as well as counting the ratio of 2P stars. However, although our simulations suffer from mass budget problem like many other simulations did, it's important to know how 2P gas released, enters, mixed and stayed within cold dense clump and eventually form the stars. In this section, we studied the impact of mixing process.

381

#### 6.1.1. Existence

382

383

384

385

In order to confirm the existence of the effect of mixing, we develop a analytical model with assumption of instaneous homogenius chemical mixing, so that the [Na/Fe] variation is modulated by the star formation histories, similar model is also developed in Shi et al. (2025). The model is based on the mass evolution of gas, stars and enriched gas(represented by Na in our work):

386

$$\begin{aligned} \frac{dM_{yield}}{dt} &= \eta DM(t - t_{yield}) \\ \frac{dM_*}{dt} &= \text{sfr}(t) \\ \frac{dM_{gas}}{dt} &= -\frac{dM_*}{dt} - \mathcal{R}_{exp} + \frac{dM_{yield}}{dt} \\ \frac{dM_{Na}}{dt} &= -\frac{M_{Na}}{M_{gas}} \left( \frac{dM_*}{dt} + \mathcal{R}_{exp} \right) + X_{Na,mean} \frac{dM_{yield}}{dt} \end{aligned} \quad (13)$$

where  $M_{yield}$ ,  $M_*$ ,  $M_{gas}$ ,  $M_{Na}$  are total stellar ejecta mass, stellar mass, gas mass within lagrangian radius and Na enrichment mass, respectively.  $X_{Na,ex}$  is the mean mass fraction of Na in the yield table, for binary yield it is about  $4 \times 10^{-6}$ .  $\mathcal{R}_{exp}$  is the instantaneous gas expulsion rate,  $DM(t - t_{yield})$  is the dying mass as a function of present time  $t$  and enrichment timescale  $t_{yield}$ , here we define

$$DM(t - t_{yield}) = \text{sfr}(t - t_{yield})$$

387 sfr( $t$ ) is a triangle-shape and integrated-SFE-normalized star formation efficiency function:

388

$$\text{sfr}(t) = \begin{cases} \frac{\varepsilon_{int} M_{cl}}{t_p - t_s} (t - t_s) & , t_s < t \leq t_p \\ \frac{\varepsilon_{int} M_{cl}}{t_p - t_s} (2t_p - t_s - t) & , t_p < t \leq 2t_p - t_s \\ 0 & , \text{else} \end{cases} \quad (14)$$

, where  $t_s, t_p$  and  $t_e$  are the time when star formation starts, peaks and ends, respectively. With gas expulsion(e.g. Krause et al. 2016; Silich & Tenorio-Tagle 2017; Goodwin & Bastian 2006), star formation histories(Li et al. 2019; Ostriker & Kim 2022; Grudić et al. 2018), and pollution timescale models equipped, in principle we are able to calculate a variation of elements abundance we are interested in. If assume the enriched gas is completely mixed with pristine gas once it is released, the spread of Na in stars will rely on their formation time  $t$  and the instantaneous mass fraction of Na  $M_{Na}(t)/M_{gas}(t)$ . Therefore, Na distribution in stars can be derived by:

$$P(X_{Na,star} = X_{Na}) = \text{sfr}(t) X_{Na,gas}(t)$$

then we can derive the upper limit of chemical difference  $\Delta[\text{Na}/\text{Fe}]_{\text{ex}}$  using the dilution model(Ricardo J. Vaca et al. 2024; Prantzos & Charbonnel 2006):

$$[\text{el}/\text{Fe}](\mathbf{f}) = \log_{10} [(1 - \mathbf{f}) \cdot 10^{[\text{el}/\text{Fe}]_{P2}} + \mathbf{f} \cdot 10^{[\text{el}/\text{Fe}]_{P1}}]$$

where

$$f = 1 - \frac{M_{Na}}{M_{gas} X_{init,Na} + M_{Na}}$$

389 . Using exponential gas expulsion(also used by Dinnbier & Walch 2020; Kroupa et al. 2001; Dinnbier & Kroupa 2020;  
390 Brinkmann et al. 2017)<sup>2</sup> and triangular-shape star formation histories(Li et al. 2019; Ostriker & Kim 2022; Grudić  
391 et al. 2018) model yields typically  $\sim \frac{1}{3}$  Na extrema variation in simulations. In practice, we use the simulation data  
392 rather than theoretic models to get maximum accuracy, since our goal is to evaluate the effect of other than mixing.  
393 We directly adopt the  $M_{gas}$  and  $M_*$  by calculating the gas retains and the stellar mass within lagrangian radius from  
394 the center of the newly born star clusters, and calculated population-average enrichment fraction from the yield  
395 table to model the Na mass fraction evolution with the infant star clusters, no enriched gas outflow is assumed, and  
396 eventually we derive the [Na/Fe] range of the model which is marked as the errorbars and dash lines in Fig. ???. The

<sup>2</sup> this formula could not well fit the gas evolution of our simulations due to the simplifying assumption neglects the radiation-pressure dominated initial phase of gas expansion(Brinkmann et al. 2017)

maximum stellar [Na/Fe] of all our simulation have reached an order of [Na/Fe]  $\sim 0.8$ , except for the most diffuse one(M1e6R100L0E1). The range of [Na/Fe](max minus min) of simulation is larger than what instantaneous mixing model predicted by a factor of  $\sim 10$ , the magnitude is even more severe for more diffuse and yield boosted GMCs, up to 100 times wider [Na/Fe] range. which provides a proof for the existence of spatially and temporally inhomogeneous mixing.

In the rest of this section, we are going to present some metrics that are able to quantize the inhomogeneous mixing within the proto-clusters during star formation and its relation to the mean stellar Na abundance.

#### 6.1.2. Diffusion on phase diagram

To further investigate the inhomogeneous mixing evidenced by the enhanced [Na/Fe] spread, we analyze the diffusion of enriched gas using phase diagrams. This approach allows us to visualize how gas phases evolve during star formation and interact with enrichment sources. We begin by defining the key gas phases and the criteria for star formation. Closely following Deng et al. (2024), we adopt a temperature-based partitioning of the ISM into the following phases: cold neutral medium (CNM), defined as  $T < 100$  K with an extra density selection  $n > 10^4 \text{ cm}^{-3}$  introduced to preferentially select star-forming sub-structures; warm neutral medium (WNM),  $100 \text{ K} < T < 8000 \text{ K}$ ; warm ionized medium (WIM),  $8000 \text{ K} < T < 10\,000 \text{ K}$ ; and hot ionized medium (HIM),  $T > 10\,000 \text{ K}$ . For the purposes of star-formation modeling, star-forming gas refers to a subset of CNM cells that additionally satisfy criteria for high density, gravitational boundedness (self-gravitating) and converging flows. it is expected to be converted into star particles on the local free-fall timescale  $\sim \Delta t/t_{\text{ff}}$  in RIGEL code.

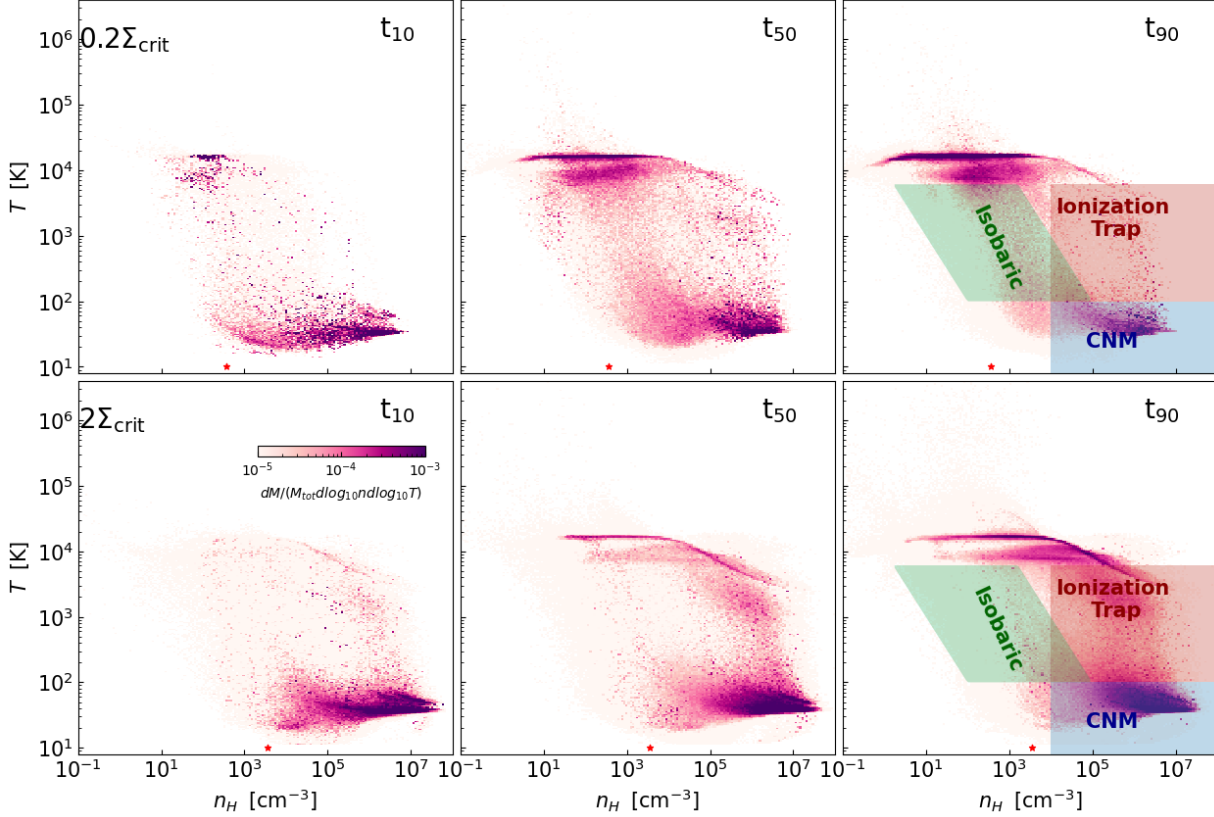
Figure 12 displays the Na mass increment(final-initial) weighted phase diagram of gas, with the left, middle, and right columns corresponding to simulations at 10%, 50%, and 90% mass assembly epochs (i.e.,  $t_{10}$ ,  $t_{50}$ ,  $t_{90}$ ), respectively. The motion of enriched gas is clearly traceable in this diagram. Initially, MIB releases enriched gas into adjacent regions, where it rapidly mixes with cold, dense gas. A portion of this enriched gas is then heated and ionized by stellar feedback, leading to the appearance of enrichment signals in the  $10^4$  K regions on the phase diagram. The transition between the cold neutral medium (CNM) and the radiation ionized zone( $T \sim 10^4$  K) illustrates the dominant pathway for pollutants to escape star-forming regions: Pollutants preferentially enrich the densest CNM(this may due to our the zero yielding timescale setting), for the diffuse GMCs( $\Sigma_0 < \Sigma_{\text{crit}}$ , the upper row in Figure 12), the enriched gas tend to escape from CNM zone along an isobaric track ( $T \propto n^{-1}$ ), where the gas could keep thermal equilibrium, while for the dense GMCs( $\Sigma_0 > \Sigma_{\text{crit}}$ , see the lower row in Figure 12), the enriched gas tend to directly ionized by the radiation without significant expansion.

Figure 13 shows the ratio of Na increment fraction of Isobaric track zone to that of ionization trap zone. The solid lines are the simulations with zero yield lag, unity yield boost factor color-coded by their initial surface density in unit of  $\Sigma_{\text{crit}}$ , the short dash lines in the right end of the figure are their time-averaged values. the mass ratio of enriched gas escape through isobaric track to that through gravitation bounded zone decrease as the increasing GMCs' initial surface density, the turning point( $f_p/f_i \approx 1$ ) is at about  $\Sigma_{\text{crit}}$ . This suggests that the CNM gas being heated in a nearly isochoric manner and departing from the star-forming regions, when the GMC is gravitation-dominated, while the CNM in the more diffuse giant molecular clouds escapes along a path of thermal equilibrium. No significant discrepancy between dash and solid lines with the same color proves that yield boost factor does not play an important role in changing the thermodynamic of the enriched gas. We also plot a pairs of simulation to illustrate the influence of yielding timescale on the phase diagram weighted by Na enrichment("M1e15L0E20" in thick solid line vs. "M1e5R15LNE20" in dotted line). The earlier the enrichment occurs, the more the enriched gas tends to be injected into the cold, dense phases of the interstellar medium (ISM), thereby leading to a higher 2P star formation.

Do the escape rates of these two channels differ? If so, could they contribute to 2P formation? To address this question, we first calculate the net cooling timescale, defined as the difference between the thermal energy per H and its upper thermal limit( $T > T_{\text{up,CNM}} = 100$  K), divided by the net cooling rate per H atom:

$$t_{\text{cool}} = \frac{k_B T_{\text{up,CNM}} - \langle U \rangle}{\langle \Lambda_{\text{net}} \rangle}, \quad \langle U \rangle = \frac{\sum_i U_i}{\sum_i n_i V_i}, \quad \langle \Lambda_{\text{net}} \rangle = \frac{\sum_i n_i^2 \Lambda_{\text{net}} V_i}{\sum_i n_i V_i} \quad (15)$$

where subscript i denotes i-th CNM particle,  $n_i$  is its number density,  $V_i$  its volume,  $\Lambda_{\text{net}}$  the net cooling rate, and  $U$  the thermal energy. This metric represents the time required for CNM to leave the star-forming region due to



**Figure 12.** Na mass-increment (final – initial) weighted phase diagrams of the gas. Columns show three assembly epochs ( $t_{10}, t_{50}, t_{90}$ ); rows compare diffuse ( $\Sigma_0 < \Sigma_{\text{crit}}$ , upper row) and dense ( $\Sigma_0 > \Sigma_{\text{crit}}$ , lower row) GMCs. Color indicates Na mass increment per phase bin; the diagrams trace the motion of enriched gas from cold, dense CNM into warmer/ionized phases. For diffuse clouds enriched gas tends to escape along an approximately isobaric track ( $T \propto n^{-1}$ ), while for dense clouds enrichment is more confined and shows direct ionization trapping.

heating<sup>3</sup>. Figure 14 shows the net cooling time versus mean stellar [Na/Fe], bullets are color-coded by  $\Sigma_0$  of the GMC. Strikingly, we find a strong anti-correlation between the heating timescale and the mean stellar [Na/Fe]. This result seems contradict to our expectation. Conventionally, a shorter heating timescale implies that enriched gas is rapidly heated and expelled from the Cold Neutral Medium (CNM) phase before it can be incorporated into new stars. One would expect this rapid removal to suppress the capture of pollutants, resulting in lower stellar chemical enrichment.

However, this apparent contradiction can be resolved by examining the energy budget under different gravitational potentials. As previously discussed, the shorter heating timescales are predominantly found in the most dense GMCs (e.g.,  $\Sigma_0 \sim 10^3 M_\odot/\text{pc}^2$ ). In these environments, the deep gravitational potential fundamentally alters the partition of feedback energy. Our analysis of the energy distribution reveals that in denser GMCs, a larger fraction of the injected energy is channelled into turbulent kinetic energy rather than thermal energy. Specifically, we observe that the ratio of turbulent to thermal energy rises steadily over time, and the time-averaged thermal-to-kinetic energy ratio remains significantly lower in dense GMCs compared to their diffuse counterparts. This suggests that in high- $\Sigma$  environments, gravitational confinement prevents the rapid hydrodynamic expansion of heated gas, forcing the feedback energy to drive a vigorous turbulent cascade. Consequently, the turbulent mixing timescale becomes sufficiently short relative to the gas removal timescale. The high [Na/Fe] abundance in these models serves as evidence that turbulent diffusion—which efficiently transports pollutants into star-forming cores—dominates over the suppression effect caused by thermal evaporation from the CNM.

The MP formation involves a process in which an HII region competes with a star-forming region for enriched gas.

<sup>3</sup> Note that in all our simulation samples, the CNM during the star-forming phase is, on average, in a state of net heating, i.e.  $\Lambda_{\text{net}} > 0$ . Therefore, using  $k_B T_{\text{up,CNM}} - \langle U \rangle$  as the numerator in the Eq.15 would be more reasonable, even though the notation is labeled as "cooling".

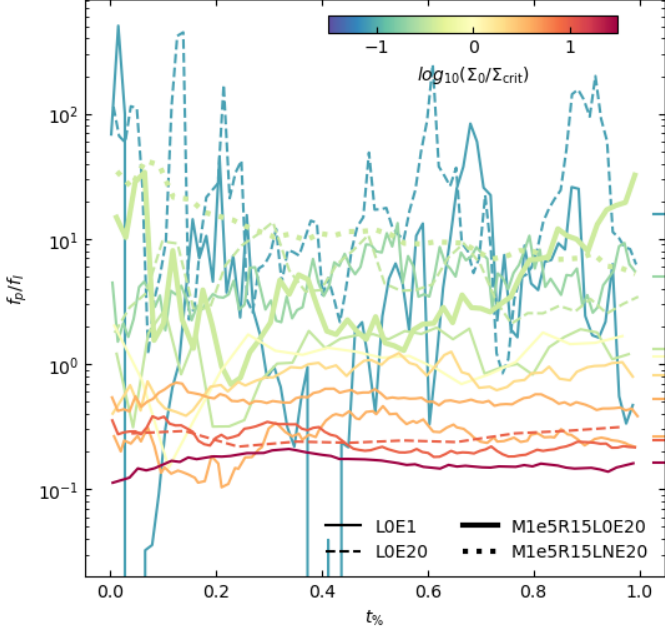


**Figure 13.** Ratio of Na increment fraction in the isobaric-track zone to that in the ionization-trap zone ( $f_p/f_i$ ) as a function of time for selected simulations. Solid lines: zero-yield-lag,  $\eta = 1$  Eq. 15) versus mean stellar [Na/Fe] for all simulations; points runs color-coded by initial surface density normalized to  $\Sigma_{crit}$ ; are color-coded by initial surface density  $\Sigma_0$ . The plot shows a short-dashed lines at the right indicate time-averaged values. The mass ratio  $f_p/f_i$  decreases with increasing  $\Sigma_0$ , with a transition near  $\Sigma_{crit}$ . Dotted/alternate curves illustrate the effect of different yielding timescales; earlier enrichment injects a larger fraction into cold, dense phases.

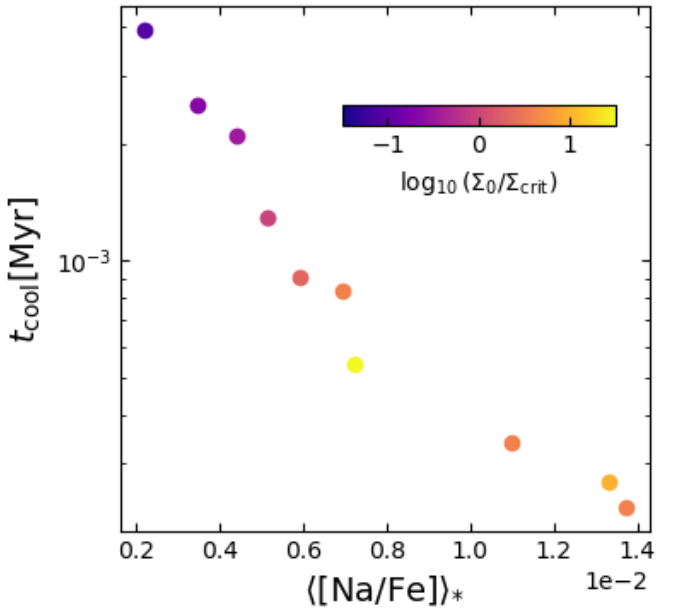


**Figure 14.** Net ‘cooling’ (heating) timescale  $t_{cool}$  (as defined in Eq. 15) versus mean stellar [Na/Fe] for all simulations; points are color-coded by initial surface density  $\Sigma_0$ . The plot shows a strong anti-correlation: shorter  $t_{cool}$  (faster net heating of CNM) is associated with higher mean stellar [Na/Fe], reflecting the role of gravitational confinement and turbulent energy partitioning in dense GMCs.

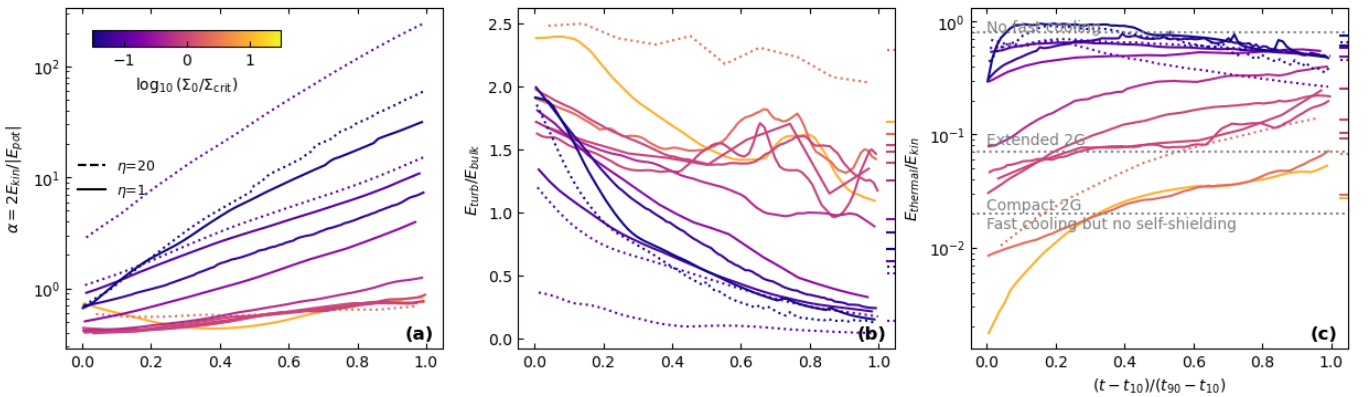


**Figure 15.** Energy partition between turbulent kinetic and thermal energy in the gas. Panels/curves (color-coded by  $\Sigma_0$  or time) show that denser GMCs channel a larger fraction of injected feedback energy into turbulent motions rather than thermal energy; this elevated turbulent/thermal ratio enhances turbulent mixing and promotes the retention of pollutants in star-forming cores, helping explain the higher [Na/Fe] observed in dense runs.

If the time required for pollutants to mix into the star-forming region exceeds the timescale over which the region becomes ionized(heated), the number of enriched stars will be significantly reduced. To quantify this competition, we calculate the average over all stars of the mean distance from each star to its 32 nearest star-forming gas cells,  $\langle L \rangle_{32}(t)$ . This metric naturally reflects both the effective radius of the larger bubble between the stellar wind and the radiation, and indicates the average distance from the contamination sources to the star-forming region. We regard

the time required for the volume of  $\langle L \rangle_{32}$  to expand to the volume of the infant star cluster as the "survival timescale" of the star-forming region, which is

$$N_*^{\frac{1}{3}}(t_{\text{fill}})\langle L \rangle_{32}(t_{\text{fill}}) = R_{\text{cl}} \quad (16)$$

, where  $N_*$  is the number of the surviving massive stars. Figure ?? shows the temporal evolution of  $\langle L \rangle_{32}$ . The gray dash scaling are the Ionization sphere radius ( $R_i \sim n^{-6/7} t^{4/7}$ , Draine 2011), effectively cooled(EC) wind bubble( $\propto n^{-1/(4-k_\rho)} t^{(d+2)/(4-k_\rho)}$ , Lachlan Lancaster et al. 2021; Lancaster et al. 2021b), self-similar wind bubble( $\propto n^{-1/(5-k_\rho)} t^{(d+2)/(5-k_\rho)}$ , Koo & McKee 1992; Krause 2003), respectively. The power law index of energy and density profile  $d$  and  $k_\rho$  are adopted from the measured parameters of our simulation. At early stage,  $\langle L \rangle_{32}$  expand in the same way as those bubble do, some of the GMCs change their expansion model after bubble merged( $t > t_{\text{fill}}$ ). In addition, a diffusion timescale can be defined to represent the typical time for 2P ejecta encounter and mix with the pristine cold dense gas:

$$\tau_{\text{diffu}}(t) = \frac{\langle L \rangle_{32}(t)}{v_{\text{rms}}(t)} \quad (17)$$

, where  $v_{\text{rms}}$  is the density-weighted root mean square velocity.

In summary, when the  $\Sigma_0$  of a GMC exceeds  $\Sigma_{\text{crit}}$ , the gravitational potential well strongly suppresses the expansion work done by stellar feedback on the cloud (see Figure 12). Under such constrained conditions, the injected energy finds it more difficult to escape as large-scale mechanical work via PdV, instead, a larger fraction is transferred into turbulent kinetic energy and cascades down to smaller scales, ultimately dissipating into thermal energy via turbulence (see Figures 15). Consequently, after being injected, enriched material (pollutants) is first entrained by turbulence and diffuses toward smaller scales along the turbulent cascade. If, during this process, turbulent dissipation raises its temperature or ionization degree beyond the threshold for star-forming phases, this portion of enriched material will detach from the cold, dense star-forming gas and fail to be incorporated into the next generation of stars.

Surprisingly, we find that the average sodium (Na) abundance in the resulting stars positively correlates with the "net cooling timescale per H atom" of the gas in the star-forming region (which is typically positive in our simulations, i.e., effectively a heating timescale). Notably, in the two sets of simulations around  $\Sigma_0 \sim 10^3 M_\odot \text{pc}^2$  ("M1e6R15L0E1" and "M1e7R30L0E1"), due to an exceptionally strong IR field and significantly enhanced dust heating, the average stellar Na abundance in these clouds is higher than in denser GMCs. Based on the physical chain described above, we interpret this as follows: the local heating rate reflects both the rate at which enriched material leaves the CNM (or becomes ionized/heated and loses eligibility for star formation) and the intensity of the turbulent cascade and dissipation. The observed average Na abundance suggests that, in most cases, the diffusion and redistribution induced by the turbulent cascade have a more significant impact on the incorporation of enriched material into stars than the direct loss of gas back to the large-scale ISM due to heating/ionization.

The next section will focus on quantifying the spatial and temporal scales of enriched gas diffusion within cold, dense gas—including measurements of the turbulent diffusion coefficient, dissipation timescale, and mass flux—to further determine which mechanism truly dominates the formation or absence of 2P stars under different  $\Sigma_0$  conditions.

### 6.1.3. Mixing Timescales

In the above section, we utilize phase diagram, energy partition, and bubble dynamics, and related parameters to quantify how, and at what rate, could enriched gas escape from star-forming regions, which primarily illustrate the competition between the cool and hot phases for the enriched gas. Within the cold-phase gas itself, the coupling between star formation and the turbulent mixing of enriched gas also significantly influences the 2P ratio. In idealized scalar mixing experiments, contaminants are typically released either from a single source or are assumed to have a uniform abundance. However, in our realistic star formation simulations, defining a baseline for mixing(i.e. a completely unenriched abundance) is really problematic, due to its dependence on not only the IMF but also the yield model employed. Therefore, following Liubin Pan (????), we define the primordial fraction  $P$  as the mass fraction of the gas whose  $[\text{Na}/\text{Fe}] - [\text{Na}/\text{Fe}]_{\text{init}} < 0.0002$ . Then the time evolution of primordial fraction of ISM can be written as(Liubin Pan ????)

$$P(t) = \frac{1}{1 + \frac{\tau_{\text{mix}}}{\tau_{\text{src}}} e^{t/\tau_{\text{mix}}}} \quad (18)$$

where  $\tau_{\text{mix}}$  is the time for turbulence to stretch the element tracers to the diffusion scale,  $\tau_{\text{src}}$  is a characteristic time for primordial gas passed through stars that became the enriched ejecta:

$$\tau_{src} = \frac{M_g}{\text{sfr}(t)f_{yield}} \approx \frac{1 - \varepsilon_{int}}{f_{yield}\eta\varepsilon_{int}}\tau_{dur} \quad (19)$$

, where  $\text{sfr}(t)$  is the star formation rate and  $f_{yield} = 0.0345$  is the IMF-averaged returned fraction from polluters,  $\eta$  is the boost factor of chemical yield(see 3 for details). Figure ?? shows the source timescale and mixing timescale as the function of surface density. Their relations towards surface density can be fitted with the following formulas:

$$\lg(\tau_{mix}) = -0.66 \lg \Sigma_0 + 1.56 \quad (20)$$

$$\lg(\tau_{src}) = -0.73 \lg \Sigma_0 + 2.83 \quad (21)$$

, a surface-density-independant relation  $\tau_{mix} \approx 0.3\langle\tau_c\rangle_t$  is also found, where  $\langle\tau_c\rangle_t$  is the time-average concentration dissipation timescale, which is used to capture the linear extent of the region within scalars are appreciably correlated(Pan 2008; Liubin Pan & Scannapieco 2010; Batchelor, George Keith. 1953)

$$R_X(r) = \langle X(x)X(x+r) \rangle, \quad L_X \equiv \frac{\int R_X(r)dr}{R_X(0)}, \quad \tau_c \equiv \frac{L_c^{2/3} L_v^{1/3}}{v_t} \quad (22)$$

, where  $X$  is a passive scalar field, in Eq.22 it is  $X = c$  for concentration and  $X = v$  for velocity,  $R_X(r)$  is the two-point correlation function of the scalar field,  $L_X$  is the scalar correlation length of the corresponding scalar field,  $v_t$  is the turbulent velocity scale, here we use tangential velocity to represent it, in order to avoid the contamination by bulk motion of the flow. This metric represents the time needed for the concentration cascading into a smaller characteristic length scale. That scaling relation is similar to the measurement made in theoretical models(e.g. Janicka et al. 1979; Curl 1963). An approximate estimation of  $\tau_{src}$  introduces a systematic bias related to the initial density, resulting in a discrepancy in the scaling relation between  $\tau_{src}$  and the  $\Sigma_0$  in Equation 19. An additional relation of  $\propto \rho^{1/3}$  could be incorporated to reconcile this discrepancy, i.e.  $\frac{\tau_{src,fit}}{\tau_{src}} \sim \rho_0^{1/3}$ . This scaling relation, which shows the dimension of the mean molecular distance, might implies the discrepancy stems from the insufficient consideration of dynamical processes, such as expansion during star formation, in the model proposed by Pan (2008). Now both  $\tau_{src}$  and  $\tau_{mix}$  are expressed as the parameter which is either calculable from one snapshot, or predictable by star formation or chemical yield model, in principle we are able to model the instantaneous mixing or source timescale  $\tau_{src}(t)$  and  $\tau_{mix}(t)$ . Consequently, we can define the 2P maintenance timescale as the time required for the ratio of the total mass of pristine gas involved in the mixing process to the total mass of pure 2P gas to reach the 2P threshold( $[\text{Na}/\text{Fe}] = 0.3$  in this work):

$$\tau_{2P} = \ln \left[ \left( \frac{1}{P'} - 1 \right) \frac{\tau_{src}}{\tau_{mix}} \right] \tau_{mix} \quad (23)$$

where  $1 - P'$  is the mas fraction of the pristine gas(100% pure 1P gas) that has been involved in mixing. This timescale should be regarded as the upper limits of the 2P formation, i.e.

$$\tau_{spread} + \tau_{cool} + t_{ff,CNM} = \tau_{sf} < \tau_{2P} \quad (24)$$

Assuming diffusivity, heating efficiency and CNM density are all independant on chemical abundance, then the volume 2P gas fraction is only related to the diffusion process

$$f_2(t) = \frac{M_{2P,CNM}}{M_{CNM}} = \frac{V_{2P,CNM}}{V_{CNM}} \propto \left( \frac{t}{\tau_c} \right)^{3/2} \quad (25)$$

where  $V_{2P,CNM}$  denotes the total volume of gas whose  $[\text{Na}/\text{Fe}] > 0.3$ , typically  $f_2(t) \approx f_2(\tau_{sf}(t))$ , and the stellar 2P mass fraction is

$$dM_{*,2P}(t)/dt = \text{sfr}(t)f_2(t) \quad (26)$$

where  $f_{CNM}(t)$  is the mass fraction of CNM, which can be fitted by simulation data.

## 7. DISCUSSION

### 7.1. What simulation has told us

Following the approach of using binary stars as polluters, we have simulated globular cluster formation and examined the resulting multiple-population properties. Consistent with other multi-generation scenarios, our models suffer from

the mass-budget problem: even when adopting high polluter yields corresponding to stars in the  $8\text{--}100 M_{\odot}$  range, the total mass of processed material remains insufficient to account for the observed fraction of 2P stars. Nevertheless, the simulations reveal that the mass and surface density (or radius) of the progenitor giant molecular cloud (GMC) — via their control of turbulent mixing, energy cycling (heating and cooling), and related processes — strongly influence the emergent stellar abundance distributions and the fraction of enriched material that becomes locked into stars. Crucially, despite the global mass-budget shortfall, spatially and temporally inhomogeneous enrichment can still produce stars whose Na abundances approach the mean or even the maximum of the adopted enrichment prescription.

More specifically, clusters formed from low-surface-density GMCs tend to exhibit a relatively flat high-[Na/Fe] tail among 2P stars; in some such clusters inefficient mixing produces discrete 2P subpopulations in the Na–O plane, in agreement with observations. By contrast, higher-surface-density GMCs — while showing larger mean [Na/Fe] — display a high-[Na/Fe] tail whose frequency falls off rapidly toward higher enrichment, indicative of more thorough mixing. Taken together, these results imply that an absolute abundance ceiling does not by itself rule out multi-population formation models; the remaining challenge is primarily the 1P/2P number ratio. Under the most favorable timing for enrichment (i.e., enrichment occurring immediately after star formation), stellar [Na/Fe] can reach 4–7 times the gas-phase value; if the mass of enriched material is increased while the polluter spatial distribution is held fixed, this amplification can reach factors of tens. Denser GMCs show higher utilization efficiencies of enriched material: GMCs at or above a critical surface density ( $\Sigma_{crit}$ ) can incorporate more than  $\sim 50\%$  of the enriched gas into stars. In our suite the maximum recorded efficiency was  $\sim 75\%$ , attained in a  $\Sigma_{crit}$  “boosted” GMC run.

The time-budget for star-formation–driven enrichment provides a strong constraint on initial conditions and polluter models for multiple-population formation. When we include multiple stellar feedback channels — in particular radiative feedback — the momentum injection into the gas increases by roughly a factor of five compared to a wind-only treatment. Under the requirement that a nascent cluster remain bound ( $\varepsilon_{int} 30\%$ ), only of order 2–3 Myr is available for 1P stars to enrich the surrounding ISM. This short timescale pushes the required polluter masses to  $\sim 10^2 M_{\odot}$ , making very massive stars (VMS) one of the most viable candidates to satisfy the timing constraint. Phase diagram color-coded by Na mass fraction difference (Fig. 12) indicates that the enriched gas in our GMCs are likely to be injected to the CNM and soon be heated by radiation feedback. Note that our model assume an instantaneous release of the enriched material, which might be the culprit of the significantly higher [Na/Fe] in star than that in gas (See Fig. 5), zero yield lag ensures that the bulk of the processed material is released within the star-forming regions and is efficiently accreted by new star particles before being encompassed by Strömgren spheres. This configuration represents the optimal scenario for star formation. Deviating from this specific delay would likely decrease the overlap between the domain of maximum enrichment and the loci of star formation in the phase diagram, resulting in a higher retention of enriched material in the ambient gas. Therefore, our results should be interpreted as providing an upper bound on the fraction of second-population stars achievable for a fixed polluter mass budget.

## 7.2. Possible solutions of MP

If the mass-budget constraint is also to be satisfied, a top-heavy IMF (Prantzos & Charbonnel 2006) is a plausible possibility. Recent JWST observations showing ultraviolet excesses and strong nitrogen emission in some high-redshift objects have been interpreted as consistent with a top-heavy IMF and the presence of VMS (e.g. Vink 2023), lending observational motivation to this scenario. However, our calculations indicate that even assuming optimistic yields — e.g., binaries in the  $8\text{--}100 M_{\odot}$  range ejecting  $\sim 80\%$  of their mass as processed material — one can produce at most  $\approx 6\%$  2P stars. In other words, within the framework of isolated, conventional GMC evolution it remains difficult to resolve the mass-budget problem.

External processes that prolong the duration of star formation, for example cloud–cloud collisions or sustained inflow, can help on two fronts: they relax the minimum polluter-mass required by providing a longer enrichment window, and they naturally remove a large fraction of 1P stars from the bound system. Our preliminary cloud–collision runs already demonstrate aspects of this behaviour. Combining such dynamical/assembly-driven mechanisms with rapid, high-yield polluters therefore constitutes a promising pathway for multiple-population formation. One aim of the present work is to provide a theoretical foundation for multiple-population formation in interacting GMCs and to facilitate subsequent explorations of the relevant parameter space.

## 7.3. Limitations and future perspectives

could not model multibody interaction due to the limits of the RIGEL framework, we don't have accurate stellar dynamic. In the upcoming RIGEL-2 and Arepo-N, it would be a possible improvement.

607 Note that we do not actually evolve binaries in Arepo, the only thing we concern is the pre-SN chemical yield of  
 608 the whole binary population, rather than the chemical enrichment or other properties of individual binary system.  
 609 We omit the effect of the multibody interaction, which has been proved not significantly change the binary fraction,  
 610 seperation distribution of massive binaries, so that the evolution of binary is completely determined by its initial  
 611 parameter. Despite multibody interaction could [Cournoyer-Cloutier et al. \(2024\)](#)  
 612 non-interactive: wind roche lobe

613 In addition, the rotation due to the accretion or merger will also rejuvenate the stars, according to [De Mink et al.](#)  
 614 (2009), the secondary will reach its critical rotation after first time mass transfer, and the critical rotation will elongate  
 615 its age by  $\sim 40\%$  for massive stars(See figure 4 in [Georgy et al. 2013](#)). However, the spin of stars are highly related to  
 616 the binary interactions like mass transfer and tide(see e.g. [S. E. De Mink et al. 2013](#)). Semi-analytical model of it is  
 617 still needed. We will consider the chemical yield of fast rotating stars(e.g. [Nandal et al. 2024](#)) in our future work.

618 Binary interaction will cause SNe feedback delayed and displace ([Wagg et al. 2025](#)), their effect on star formation  
 619 and MP formation will be investigated in our upcoming work.

620 While our model provides a detailed accounting of the chemical budget from massive binaries, several simplifications  
 621 regarding stellar dynamics and binary physics warrant discussion.

622 First, the stellar dynamics in our current framework are treated approximately. In the Arepo-RIGEL simulations,  
 623 star particles represent individual stars or small stellar populations that interact gravitationally with the gas and dark  
 624 matter, but we do not resolve the direct, discrete N-body gravitational encounters that characterize the dense cores  
 625 of globular clusters. Consequently, our model does not capture multi-body interactions (e.g., three-body exchanges,  
 626 fly-bys), which can harden binaries, disrupt soft systems, or alter orbital parameters dynamically. We note, however,  
 627 that recent direct N-body studies suggest that the binary fraction and semi-major axis distribution of *massive* stars are  
 628 not significantly altered by dynamical processing during the early cluster formation phase ([Cournoyer-Cloutier et al.](#)  
 629 [2024](#)). Therefore, we expect the initial parameter distribution sampled in our model to remain a valid approximation  
 630 for the early enrichment phase. Future iterations of our code, such as the upcoming RIGEL-2 or Arepo-N frameworks,  
 631 aim to incorporate accurate N-body integrators to fully capture the interplay between cluster dynamics and binary  
 632 evolution.

633 Second, our treatment of binary evolution pathways relies on semi-analytic prescriptions rather than direct hydro-  
 634 dynamical evolution of the binary systems. We sample the pre-supernova chemical yields based on initial parameters  
 635 and assume the evolution is strictly determined by these initial conditions. This approach necessitates classifying  
 636 systems into discrete channels (e.g., stable RLOF vs. CE). As a result, we treat systems that do not fill their Roche  
 637 lobes as effectively single stars. This likely leads to a conservative estimate of enrichment, as it neglects intermediate  
 638 interaction modes such as Wind-Roche Lobe Overflow (WRLOF; e.g., ?), which can facilitate mass transfer in wider  
 639 binaries that do not formally meet the RLOF criteria.

640 Finally, this work focuses primarily on the chemical consequences of binaries (the mass budget problem), treating  
 641 the feedback consequences as secondary. While we account for the modified chemical yields and the adjusted lifetimes  
 642 (rejuvenation), binary interactions can also fundamentally alter the spatial distribution of feedback. For instance,  
 643 [Wagg et al. \(2025\)](#) demonstrated that binary kicks and delayed supernovae can cause explosions to occur in lower-  
 644 density environments, significantly changing the momentum coupling and thermal efficiency of the feedback. In this  
 645 work, we have not explicitly modeled the kinematic kicks associated with binary hardening or supernova recoil. A  
 646 comprehensive study investigating how the delayed and displaced feedback from binaries impacts the hydrodynamics  
 647 of cloud collapse and star cluster formation will be presented in our upcoming work.

## 648 8. CONCLUSION

649 This paper performed a suites of cluster formation simulations in order to investigate what conditions faver the  
 650 formation of multiple stellar popullations in globular clusters. We built a binary yield model base on the framework  
 651 of Arepo-RIGEL model,

652 Main findings of our work are listed as follow:

- 653 1. There is no chance for a normal GMC to form MP through normal star formation process
- 654 2. Under the minimum yielding lag, the uniform abundances distribution of 2P stars is easy to build, diffuser GMC  
 655 shows tend to have more flatten [Na/Fe] distribution, discreteness appears on serveral most diffuse GMCs,impling  
 656 a highly insufficient turbulent mixing process.

657 3. On the two ends of the GMC show distinctive escape channels for enriched gas, for the denser

We thank all the people that have made this AASTeX what it is today. This includes but not limited to Bob Hanisch, Chris Biemesderfer, Lee Brotzman, Pierre Landau, Arthur Ogawa, Maxim Markevitch, Alexey Vikhlinin and Amy Hendrickson. Also special thanks to David Hogg and Daniel Foreman-Mackey for the new "modern" style design. Considerable help was provided via bug reports and hacks from numerous people including Patricio Cubillos, Alex Drlica-Wagner, Sean Lake, Michele Bannister, Peter Williams, and Jonathan Gagne.

## APPENDIX

## A. BINARY SAMPLING PROCEDURE

The Coefficient  $a_i$  is polynomial fitted by metallicity in solar  $\zeta \equiv \log_{10}(Z/0.02)$ , and the coefficients are listed below(see Table 2).

**Table 2.** Coefficient of  $t_{BGB}$

	$\zeta^0$	$\zeta^1$	$\zeta^2$	$\zeta^3$
$a_1$	1593.890	2053.038	1231.226	232.7785
$a_2$	2706.708	1483.131	577.2723	7.411230
$a_3$	146.6143	-104.8442	-6.795374	-1.391127
$a_4$	0.04141960	0.04564888	0.02958542	0.005571483
$a_5$	0.3426349	—	—	—

## REFERENCES

- 669 Bastian, N., Lamers, H. J. G. L. M., De Mink, S. E., et al.  
670 2013, Monthly Notices of the Royal Astronomical Society,  
671 436, 2398, doi: [10.1093/mnras/stt1745](https://doi.org/10.1093/mnras/stt1745)

672 Bastian, N., & Lardo, C. 2018, Annual Review of  
673 Astronomy and Astrophysics, 56, 83,  
674 doi: [10.1146/annurev-astro-081817-051839](https://doi.org/10.1146/annurev-astro-081817-051839)

675 Batchelor, George Keith. 1953, The Theory of  
676 Homogeneous Turbulence (Cambridge university press)

677 Baumgardt, H., & Hilker, M. 2018, Monthly Notices of the  
678 Royal Astronomical Society, 478, 1520

679 Birk Zimmermann, Walch, S., Clarke, S. D., Wünsch, R.,  
680 & Klepitko, A. 2025, Monthly Notices of the Royal  
681 Astronomical Society, 544, 2136,  
682 doi: [10.1093/mnras/staf1868](https://doi.org/10.1093/mnras/staf1868)

683 Brinkmann, N., Banerjee, S., Motwani, B., & Kroupa, P.  
684 2017, Astronomy & Astrophysics, 600, A49,  
685 doi: [10.1051/0004-6361/201629312](https://doi.org/10.1051/0004-6361/201629312)

686 Brott, I., De Mink, S. E., Cantiello, M., et al. 2011,  
687 Astronomy & Astrophysics, 530, A115,  
688 doi: [10.1051/0004-6361/201016113](https://doi.org/10.1051/0004-6361/201016113)

689 Carretta, E., Bragaglia, A., Gratton, R. G., et al. 2009,  
690 Astronomy & Astrophysics, 505, 117,  
691 doi: [10.1051/0004-6361/200912096](https://doi.org/10.1051/0004-6361/200912096)

692 Chen, X., Liu, Z., & Han, Z. 2024, Progress in Particle and  
693 Nuclear Physics, 134, 104083,  
694 doi: [10.1016/j.ppnp.2023.104083](https://doi.org/10.1016/j.ppnp.2023.104083)

695 Cournoyer-Cloutier, C., Tran, A., Lewis, S., et al. 2021,  
696 Monthly Notices of the Royal Astronomical Society, 501,  
697 4464, doi: [10.1093/mnras/staa3902](https://doi.org/10.1093/mnras/staa3902)

698 Cournoyer-Cloutier, C., Sills, A., Harris, W. E., et al. 2024,  
699 Massive Star Cluster Formation with Binaries. I.  
700 Evolution of Binary Populations, arXiv.  
701 <https://arxiv.org/abs/2410.07433>

702 Curl, R. L. 1963, AIChE journal, 9, 175

703 De Mink, S. E., Pols, O. R., Langer, N., & Izzard, R. G.  
704 2009, Astronomy & Astrophysics, 507, L1,  
705 doi: [10.1051/0004-6361/200913205](https://doi.org/10.1051/0004-6361/200913205)

706 Decressin, T., Meynet, G., Charbonnel, C., Prantzos, N., &  
707 Ekström, S. 2007, Astronomy & Astrophysics, 464, 1029,  
708 doi: [10.1051/0004-6361:20066013](https://doi.org/10.1051/0004-6361:20066013)

- 709 Deng, Y., Li, H., Kannan, R., et al. 2023, Monthly Notices  
 710 of the Royal Astronomical Society, 527, 478,  
 711 doi: [10.1093/mnras/stad3202](https://doi.org/10.1093/mnras/stad3202)
- 712 Deng, Y., Li, H., Liu, B., et al. 2024, RIGEL: Simulating  
 713 Dwarf Galaxies at Solar Mass Resolution with Radiative  
 714 Transfer and Feedback from Individual Massive Stars,  
 715 arXiv. <https://arxiv.org/abs/2405.08869>
- 716 Dinnbier, F., & Kroupa, P. 2020, Astronomy &  
 717 Astrophysics, 640, A84,  
 718 doi: [10.1051/0004-6361/201936570](https://doi.org/10.1051/0004-6361/201936570)
- 719 Dinnbier, F., & Walch, S. 2020, Monthly Notices of the  
 720 Royal Astronomical Society, 499, 748,  
 721 doi: [10.1093/mnras/staa2560](https://doi.org/10.1093/mnras/staa2560)
- 722 Draine, B. T. 2011, Physics of the Interstellar and  
 723 Intergalactic Medium, Princeton Series in Astrophysics  
 724 (Princeton, N.J: Princeton University Press)
- 725 Fall, S. M., Krumholz, M. R., & Matzner, C. D. 2010, The  
 726 Astrophysical Journal Letters, 710, L142
- 727 Fukui, Y., Habe, A., Inoue, T., Enokiya, R., & Tachihara,  
 728 K. 2020, Cloud-Cloud Collisions and Triggered Star  
 729 Formation, doi: [10.1093/pasj/psaa103](https://doi.org/10.1093/pasj/psaa103)
- 730 Ge, H., Hjellming, M. S., Webbink, R. F., Chen, X., & Han,  
 731 Z. 2010, 717
- 732 Ge, H., Webbink, R. F., Chen, X., & Han, Z. 2020a, The  
 733 Astrophysical Journal, 899, 132,  
 734 doi: [10.3847/1538-4357/aba7b7](https://doi.org/10.3847/1538-4357/aba7b7)
- 735 Ge, H., Webbink, R. F., & Han, Z. 2020b, The  
 736 Astrophysical Journal Supplement Series, 249, 9,  
 737 doi: [10.3847/1538-4365/ab98f6](https://doi.org/10.3847/1538-4365/ab98f6)
- 738 Ge, H., Tout, C. A., Chen, X., et al. 2024, The  
 739 Astrophysical Journal, 975, 254,  
 740 doi: [10.3847/1538-4357/ad7ea6](https://doi.org/10.3847/1538-4357/ad7ea6)
- 741 Georgy, C., Ekström, S., Granada, A., et al. 2013,  
 742 Astronomy & Astrophysics, 553, A24,  
 743 doi: [10.1051/0004-6361/201220558](https://doi.org/10.1051/0004-6361/201220558)
- 744 Glebbeek, E., Gaburov, E., Portegies Zwart, S., & Pols,  
 745 O. R. 2013, Monthly Notices of the Royal Astronomical  
 746 Society, 434, 3497, doi: [10.1093/mnras/stt1268](https://doi.org/10.1093/mnras/stt1268)
- 747 Glebbeek, E., Pols, O. R., & Hurley, J. R. 2008, Astronomy  
 748 & Astrophysics, 488, 1007,  
 749 doi: [10.1051/0004-6361:200809930](https://doi.org/10.1051/0004-6361:200809930)
- 750 Glen H Hunter, Clark, P. C., Glover, S. C. O., & Klessen,  
 751 R. S. 2023, Monthly Notices of the Royal Astronomical  
 752 Society, 519, 4152, doi: [10.1093/mnras/stac3751](https://doi.org/10.1093/mnras/stac3751)
- 753 Gnedin, N. Y., & Abel, T. 2001, New Astronomy, 6, 437,  
 754 doi: [10.1016/S1384-1076\(01\)00068-9](https://doi.org/10.1016/S1384-1076(01)00068-9)
- 755 Goodwin, S. P., & Bastian, N. 2006, Monthly Notices of the  
 756 Royal Astronomical Society, 373, 752,  
 757 doi: [10.1111/j.1365-2966.2006.11078.x](https://doi.org/10.1111/j.1365-2966.2006.11078.x)
- 758 Gratton, R., Bragaglia, A., Carretta, E., et al. 2019, The  
 759 Astronomy and Astrophysics Review, 27, 8,  
 760 doi: [10.1007/s00159-019-0119-3](https://doi.org/10.1007/s00159-019-0119-3)
- 761 Gratton, R., Sneden, C., & Carretta, E. 2004, Annual  
 762 Review of Astronomy and Astrophysics, 42, 385,  
 763 doi: [10.1146/annurev.astro.42.053102.133945](https://doi.org/10.1146/annurev.astro.42.053102.133945)
- 764 Grudić, M. Y., Hopkins, P. F., Faucher-Giguère, C.-A.,  
 765 et al. 2018, Monthly Notices of the Royal Astronomical  
 766 Society, 475, 3511, doi: [10.1093/mnras/sty035](https://doi.org/10.1093/mnras/sty035)
- 767 Grudić, M. Y., & Guszejnov, D. 2021, MakeCloud, 1.0.  
 768 <https://github.com/mikegrudic/MakeCloud>
- 769 Gutcke, T. A., Pakmor, R., Naab, T., & Springel, V. 2021,  
 770 Monthly Notices of the Royal Astronomical Society,  
 771 staa3875, doi: [10.1093/mnras/staa3875](https://doi.org/10.1093/mnras/staa3875)
- 772 Heger, A., Fryer, C. L., Woosley, S. E., Langer, N., &  
 773 Hartmann, D. H. 2003, The Astrophysical Journal, 591,  
 774 288, doi: [10.1086/375341](https://doi.org/10.1086/375341)
- 775 Heger, A., & Woosley, S. E. 2002, The Astrophysical  
 776 Journal, 567, 532
- 777 Hurley, J. R., Pols, O. R., & Tout, C. A. 2000, Monthly  
 778 Notices of the Royal Astronomical Society, 315, 543,  
 779 doi: [10.1046/j.1365-8711.2000.03426.x](https://doi.org/10.1046/j.1365-8711.2000.03426.x)
- 780 Janicka, J., Kolbe, W., & Kollmann, W. 1979
- 781 Jenny J. Kim, & Lee, Y.-W. 2018, The Astrophysical  
 782 Journal, 869, 35, doi: [10.3847/1538-4357/aaec67](https://doi.org/10.3847/1538-4357/aaec67)
- 783 Jiang, D., Han, Z., & Li, L. 2014, The Astrophysical  
 784 Journal
- 785 Julia Roman-Duval, Jackson, J. M., Heyer, M., Rathborne,  
 786 J., & Simon, R. 2010, The Astrophysical Journal, 723,  
 787 492, doi: [10.1088/0004-637X/723/1/492](https://doi.org/10.1088/0004-637X/723/1/492)
- 788 Koo, B.-C., & McKee, C. F. 1992, Astrophysical Journal v.  
 789 388, p. 103, 388, 103
- 790 Krause, M. 2003, Astronomy & Astrophysics, 398, 113,  
 791 doi: [10.1051/0004-6361:20021649](https://doi.org/10.1051/0004-6361:20021649)
- 792 Krause, M. G. H., Charbonnel, C., Bastian, N., & Diehl, R.  
 793 2016, Astronomy & Astrophysics, 587, A53,  
 794 doi: [10.1051/0004-6361/201526685](https://doi.org/10.1051/0004-6361/201526685)
- 795 Kroupa, P., Aarseth, S., & Hurley, J. 2001, Monthly  
 796 Notices of the Royal Astronomical Society, 321, 699,  
 797 doi: [10.1046/j.1365-8711.2001.04050.x](https://doi.org/10.1046/j.1365-8711.2001.04050.x)
- 798 Lachlan Lancaster, Ostriker, E. C., Kim, J.-G., & Kim,  
 799 C.-G. 2021, The Astrophysical Journal, 914, 90,  
 800 doi: [10.3847/1538-4357/abf8ac](https://doi.org/10.3847/1538-4357/abf8ac)
- 801 Lahén, N., Naab, T., & Szécsi, D. 2024, Star Clusters  
 802 Forming in a Low Metallicity Starburst – Rapid  
 803 Self-Enrichment by (Very) Massive Stars, arXiv.  
 804 <https://arxiv.org/abs/2402.09518>
- 805 Lancaster, L., Ostriker, E. C., Kim, J.-G., & Kim, C.-G.  
 806 2021a, The Astrophysical Journal Letters, 922, L3,  
 807 doi: [10.3847/2041-8213/ac3333](https://doi.org/10.3847/2041-8213/ac3333)

- 808 —. 2021b, *The Astrophysical Journal*, 914, 89,  
 809 doi: [10.3847/1538-4357/abf8ab](https://doi.org/10.3847/1538-4357/abf8ab)
- 810 Laplace, E., Justham, S., Renzo, M., et al. 2021,  
 811 *Astronomy & Astrophysics*, 656, A58,  
 812 doi: [10.1051/0004-6361/202140506](https://doi.org/10.1051/0004-6361/202140506)
- 813 Li, H., Vogelsberger, M., Marinacci, F., & Gnedin, O. Y.  
 814 2019, *Monthly Notices of the Royal Astronomical Society*,  
 815 487, 364, doi: [10.1093/mnras/stz1271](https://doi.org/10.1093/mnras/stz1271)
- 816 Liubin Pan. ????  
 817 Liubin Pan, & Scannapieco, E. 2010, *The Astrophysical  
 818 Journal*, 721, 1765, doi: [10.1088/0004-637X/721/2/1765](https://doi.org/10.1088/0004-637X/721/2/1765)
- 819 Lynnette M. Dray, & Christopher A. Tout. 2007, *Monthly  
 820 Notices of the Royal Astronomical Society*, 376, 61,  
 821 doi: [10.1111/j.1365-2966.2007.11431.x](https://doi.org/10.1111/j.1365-2966.2007.11431.x)
- 822 Maity, A. K., Inoue, T., Fukui, Y., et al. 2024, Cloud-Cloud  
 823 Collision: Formation of Hub-Filament Systems and  
 824 Associated Gas Kinematics; Mass-collecting Cone: A  
 825 New Signature of Cloud-Cloud Collision, arXiv,  
 826 doi: [10.48550/arXiv.2408.06826](https://doi.org/10.48550/arXiv.2408.06826)
- 827 McKee, C. F., & Ostriker, E. C. 2007, *Annual Review of  
 828 Astronomy and Astrophysics*, 45, 565,  
 829 doi: [10.1146/annurev.astro.45.051806.110602](https://doi.org/10.1146/annurev.astro.45.051806.110602)
- 830 Michelle Nguyen, & Sills, A. 2024, Massive Interacting  
 831 Binaries as an Enrichment Source for Multiple  
 832 Populations in Star Clusters, arXiv.  
<https://arxiv.org/abs/2405.05687>
- 833 Milone, A. P., & Marino, A. F. 2022, Multiple Populations  
 834 in Star Clusters, arXiv.  
<https://arxiv.org/abs/2206.10564>
- 835 Moe, M., & Di Stefano, R. 2017, *The Astrophysical Journal  
 836 Supplement Series*, 230, 15,  
 837 doi: [10.3847/1538-4365/aa6fb6](https://doi.org/10.3847/1538-4365/aa6fb6)
- 838 Murray, D. W., Chang, P., Murray, N. W., & Pittman, J.  
 839 2017, *Monthly Notices of the Royal Astronomical Society*,  
 840 465, 1316, doi: [10.1093/mnras/stw2796](https://doi.org/10.1093/mnras/stw2796)
- 841 Murray, N. 2011, *The Astrophysical Journal*, 729, 133,  
 842 doi: [10.1088/0004-637X/729/2/133](https://doi.org/10.1088/0004-637X/729/2/133)
- 843 Murray, N., & Chang, P. 2015, *The Astrophysical Journal*,  
 844 804, 44, doi: [10.1088/0004-637X/804/1/44](https://doi.org/10.1088/0004-637X/804/1/44)
- 845 Nandal, D., Sibony, Y., & Tsiaitsiou, S. 2024, Fast-Rotating  
 846 Massive Population-III Stars as Possible Sources of  
 847 Extreme N-enrichment in High-Redshift Galaxies, arXiv.  
<https://arxiv.org/abs/2405.11235>
- 848 Ni, Y., Li, H., Vogelsberger, M., et al. ????  
 849 Ostriker, E. C., & Kim, C.-G. 2022, *The Astrophysical  
 850 Journal*, 936, 137, doi: [10.3847/1538-4357/ac7de2](https://doi.org/10.3847/1538-4357/ac7de2)
- 851 Pan, L. 2008, Turbulent mixing of chemical elements in  
 852 galaxies (The University of Texas at Austin)
- 853 Paxton, B., Smolec, R., Schwab, J., et al. 2019, *The  
 854 Astrophysical Journal Supplement Series*, 243, 10,  
 855 doi: [10.3847/1538-4365/ab2241](https://doi.org/10.3847/1538-4365/ab2241)
- 856 Prantzos, N., & Charbonnel, C. 2006, *Astronomy &  
 857 Astrophysics*, 458, 135, doi: [10.1051/0004-6361:20065374](https://doi.org/10.1051/0004-6361:20065374)
- 858 Raffaele G. Gratton, Carretta, E., & Bragaglia, A. 2012,  
 859 *The Astronomy and Astrophysics Review*, 20, 50,  
 860 doi: [10.1007/s00159-012-0050-3](https://doi.org/10.1007/s00159-012-0050-3)
- 861 Raskutti, S., Ostriker, E. C., & Skinner, M. A. 2016, *The  
 862 Astrophysical Journal*, 829, 130
- 863 Renaud, F. 2018, *New Astronomy Reviews*
- 864 Renzini, A., D'Antona, F., Cassisi, S., et al. 2015, *Monthly  
 865 Notices of the Royal Astronomical Society*, 454, 4197,  
 866 doi: [10.1093/mnras/stv2268](https://doi.org/10.1093/mnras/stv2268)
- 867 Ricardo J. Vaca, Cabrera-Ziri, I., C, G. M., Bastian, N., &  
 868 Salaris, M. 2024, *Astronomy & Astrophysics*, 690, A199,  
 869 doi: [10.1051/0004-6361/202451285](https://doi.org/10.1051/0004-6361/202451285)
- 870 Rosdahl, J., Blaizot, J., Aubert, D., Stranex, T., & Teyssier,  
 871 R. 2013, *Monthly Notices of the Royal Astronomical  
 872 Society*, 436, 2188, doi: [10.1093/mnras/stt1722](https://doi.org/10.1093/mnras/stt1722)
- 873 S. E. De Mink, Langer, N., Izzard, R. G., Sana, H., &  
 874 De Koter, A. 2013, *The Astrophysical Journal*, 764, 166,  
 875 doi: [10.1088/0004-637X/764/2/166](https://doi.org/10.1088/0004-637X/764/2/166)
- 876 Schneider, F. R. N., Podsiadlowski, Ph., Langer, N.,  
 877 Castro, N., & Fossati, L. 2016, *Monthly Notices of the  
 878 Royal Astronomical Society*, 457, 2355,  
 879 doi: [10.1093/mnras/stw148](https://doi.org/10.1093/mnras/stw148)
- 880 Shi, Y., Dai, L., Murray, N., et al. 2025, Very Massive Stars  
 881 and High N/O: A Tale of the Nitrogen-enriched Super  
 882 Star Cluster in the Sunburst Arc, arXiv,  
 883 doi: [10.48550/arXiv.2510.15823](https://doi.org/10.48550/arXiv.2510.15823)
- 884 Sibony, Y., Shepherd, K. G., Yusof, N., et al. 2024,  
 885 *Astronomy & Astrophysics*, 690, A91,  
 886 doi: [10.1051/0004-6361/202450180](https://doi.org/10.1051/0004-6361/202450180)
- 887 Silich, S., & Tenorio-Tagle, G. 2017, *Monthly Notices of the  
 888 Royal Astronomical Society*, 465, 1375,  
 889 doi: [10.1093/mnras/stw2879](https://doi.org/10.1093/mnras/stw2879)
- 890 Soberman, G. E., & Phinney, E. S. ????  
 891 Springel, V. 2010, *Monthly Notices of the Royal  
 892 Astronomical Society*, 401, 791,  
 893 doi: [10.1111/j.1365-2966.2009.15715.x](https://doi.org/10.1111/j.1365-2966.2009.15715.x)
- 894 Steinwandel, U. P., & Goldberg, J. A. 2025, *The  
 895 Astrophysical Journal*, 979, 44,  
 896 doi: [10.3847/1538-4357/ad98ea](https://doi.org/10.3847/1538-4357/ad98ea)
- 897 Temmink, K. D., Pols, O. R., Justham, S., Istrate, A. G., &  
 898 Toonen, S. 2023, *Astronomy & Astrophysics*, 669, A45,  
 899 doi: [10.1051/0004-6361/202244137](https://doi.org/10.1051/0004-6361/202244137)
- 900 Torrey, P., Vogelsberger, M., Sijacki, D., Springel, V., &  
 901 Hernquist, L. 2012, *Monthly Notices of the Royal  
 902 Astronomical Society*, 427, 2224

- 906 Van Den Heuvel, E. P. J. 1969, The Astronomical Journal, 74, 1095, doi: [10.1086/110909](https://doi.org/10.1086/110909)
- 907 Vartanyan, D., Laplace, E., Renzo, M., et al. 2021, The Astrophysical Journal Letters, 916, L5, doi: [10.3847/2041-8213/ac0b42](https://doi.org/10.3847/2041-8213/ac0b42)
- 908 Vink, J. S. 2023, Astronomy & Astrophysics, 679, L9, doi: [10.1051/0004-6361/202347827](https://doi.org/10.1051/0004-6361/202347827)
- 909 Vogelsberger, M., Genel, S., Sijacki, D., et al. 2013, Monthly Notices of the Royal Astronomical Society, 436, 3031, doi: [10.1093/mnras/stt1789](https://doi.org/10.1093/mnras/stt1789)
- 910 Wagg, T., Dalcanton, J. J., Renzo, M., et al. 2025, Delayed and Displaced: The Impact of Binary Interactions on Core-collapse SN Feedback, arXiv, doi: [10.48550/arXiv.2504.17903](https://doi.org/10.48550/arXiv.2504.17903)
- 920 Weinberger, R., Springel, V., & Pakmor, R. 2020, The Astrophysical Journal Supplement Series, 248, 32, doi: [10.3847/1538-4365/ab908c](https://doi.org/10.3847/1538-4365/ab908c)
- 921 Wu, B., Loo, S. V., Tan, J. C., & Bruderer, S. 2015, The Astrophysical Journal, 811, 56, doi: [10.1088/0004-637X/811/1/56](https://doi.org/10.1088/0004-637X/811/1/56)
- 922 Wu, B., Tan, J. C., Nakamura, F., et al. 2017, The Astrophysical Journal, 835, 137, doi: [10.3847/1538-4357/835/2/137](https://doi.org/10.3847/1538-4357/835/2/137)
- 923 Xu, S., & Lazarian, A. 2020, The Astrophysical Journal, 890, 157, doi: [10.3847/1538-4357/ab6e63](https://doi.org/10.3847/1538-4357/ab6e63)
- 924 Xu, X.-T., Schürmann, C., Langer, N., et al. 2025, Populations of Evolved Massive Binary Stars in the Small Magellanic Cloud I: Predictions from Detailed Evolution Models, arXiv, doi: [10.48550/arXiv.2503.23876](https://doi.org/10.48550/arXiv.2503.23876)
- 925
- 926
- 927
- 928
- 929
- 930
- 931
- 932
- 933
- 934